SPECIAL COMMUNICATION

The Genesis Solar Wind Concentrator: Flight and Post-Flight Conditions and Modeling of Instrumental Fractionation

**Roger C. Wiens · Daniel B. Reisenfeld · Chad Olinger ·
Peter Wurz · Veronika S. Heber · Donald S. Burnett**

Abstract The Genesis mission Solar Wind Concentrator was built to enhance fluences of solar wind by an average of 20x over the 2.3 years that the mission exposed substrates to the solar wind. The Concentrator targets survived the hard landing upon return to Earth and were used to determine the isotopic composition of solar-wind—and hence solar—oxygen and nitrogen. Here we report on the flight operation of the instrument and on simulations of its performance. Concentration and fractionation patterns obtained from simulations are given for He, Li, N, O, Ne, Mg, Si, S, and Ar in SiC targets, and are compared with measured concentrations and isotope ratios for the noble gases. Carbon is also modeled for a Si target. Predicted differences in instrumental fractionation between elements are discussed. Additionally, as the Concentrator was designed only for ions ≤ 22 AMU, implications of analyzing elements as heavy as argon are discussed. Post-flight simulations of instrumental fractionation as a function of radial position on the targets incorporate solar-wind velocity and angular distributions measured in flight, and predict fractionation patterns for various elements and isotopes of interest. A tighter angular distribution, mostly due to better

R.C. Wiens (✉) · C. Olinger
Los Alamos National Laboratory, P.O. Box 1663, Los Alamos, NM 87545, USA
e-mail: rwiens@lanl.gov

D.B. Reisenfeld
Department of Physics and Astronomy, University of Montana, Missoula, MT 59812, USA

P. Wurz
Physikalisches Institut, University of Bern, Sidlerstrasse 5, 3012 Bern, Switzerland

V.S. Heber
Department of Earth and Space Sciences, UCLA, 595 Charles Young Drive East, Los Angeles,
CA 90095–1567, USA

D.S. Burnett
California Institute of Technology, 1200 California Boulevard, Pasadena, CA 91109, USA

spacecraft spin stability than assumed in pre-flight modeling, results in a steeper isotopic fractionation gradient between the center and the perimeter of the targets. Using the distribution of solar-wind velocities encountered during flight, which are higher than those used in pre-flight modeling, results in elemental abundance patterns slightly less peaked at the center. Mean fractionations trend with atomic mass, with differences relative to the measured isotopes of neon of $+4.1 \pm 0.9$ ‰/amu for Li, between -0.4 and $+2.8$ ‰/amu for C, $+1.9 \pm 0.7$‰/amu for N, $+1.3 \pm 0.4$ ‰/amu for O, -7.5 ± 0.4 ‰/amu for Mg, -8.9 ± 0.6 ‰/amu for Si, and -22.0 ± 0.7 ‰/amu for S (uncertainties reflect Monte Carlo statistics). The slopes of the fractionation trends depend to first order only on the relative differential mass ratio, $\Delta m/m$.

This article and a companion paper (Reisenfeld et al. 2012, this issue) provide post-flight information necessary for the analysis of the Genesis solar wind samples, and thus serve to complement the Space Science Review volume, The Genesis Mission (v. 105, 2003).

1 Introduction

The Genesis mission was proposed and executed to obtain information on the isotopic and elemental composition of the Sun, using the solar-wind as the medium (Burnett et al. 2003). Solar-wind elemental abundances and some isotope ratios have been measured by in-situ instruments, as reviewed, e.g., in Bochsler (2007), Kallenbach et al. (2007), and Wiens et al. (2004). However, in order to clearly relate solar and solar-wind isotopic compositions to those of other solar-system bodies and to primitive materials remaining from the formation of the solar system, solar-wind isotopic measurements required higher precisions and accuracies than had been obtained to date. The isotope ratios of volatile elements are of particular interest because they differ between planetary bodies and among meteorite types. Oxygen isotope ratios were found to differ by up to ~ 7 % among planetary precursor materials, displaying non-mass-dependent relationships (e.g., Clayton et al. 1977; Clayton and Mayeda 1984; Clayton 1993; Young and Russell 1998). Several different concepts (e.g., Clayton and Mayeda 1984; Thiemens and Heidenreich 1983; Clayton 2002) were put forward to explain this heterogeneity. Each of the theories implied a grossly different oxygen isotopic composition for the Sun (e.g., Wiens et al. 1999). Nitrogen isotopes also presented a mystery. But in this case the isotopic heterogeneity was most strongly displayed in lunar soils exposed to solar wind (e.g., Kerridge 1993), as well as a few anomalous meteorites (e.g., Franchi et al. 1986). The presence of widely varying (e.g., by 20 %) nitrogen isotope ratios in solar-wind-implanted lunar soils suggested that either the solar wind had itself varied in composition over time, or else another component was supplying nitrogen ions to the lunar surface (e.g., Wieler et al. 1999). Nitrogen has only two stable isotopes, so unlike oxygen it is not clear whether mass-dependent fractionation could have produced part or all of the isotopic heterogeneity. More recent measurement of nitrogen in the Jovian system (Fouchet et al. 2000; Owen et al. 2001; Atreya et al. 2003) indicated an isotopically light composition relative to the lunar soils.

To address these and other issues the Genesis solar-wind sample return mission was conceived. The mission was based on the successful Apollo Solar Wind Composition (SWC) experiments in the early 1970s in which foils of aluminum and platinum were exposed to solar wind for durations of 77 minutes to 45 hours by astronauts on the lunar surface and then returned to Earth for analysis (e.g., Geiss et al. 2004). The solar-wind, with energies typically

between 0.5 and 3.5 keV/amu, embeds itself within the top 100 nm of any substrate placed in interplanetary space. The main objective of Genesis was to expose purer substrates in a cleaner environment than the dusty lunar surface, and to expose the substrates over orders of magnitude longer time scales (Burnett et al. 2003). This was best done with a dedicated spacecraft outside of the Earth's magnetosphere for a period of years. The materials chosen as collection substrates for the Genesis mission consisted of a variety of semiconductor materials (Jurewicz et al. 2003).

The Genesis spacecraft was launched in August, 2001. It exposed its substrates for a period of 853 days (Reisenfeld et al. 2012) at the L1 Lagrangian point and then returned them to Earth. The mission was marred by a failure of the parachutes to deploy during re-entry over the desert in Utah, USA, and the resulting hard landing broke nearly all of the collectors into smaller pieces. Fortunately, many of these pieces were still usable for many of the envisioned analyses.

As the mission concept took shape, it became clear that the solar wind is so rarified that measurements of many elements and isotopes would still be very challenging even with far longer exposures than the lunar SWC experiment. Additionally, some elements tend to be ubiquitous contaminants in almost every material on Earth. Oxygen is one such element, as it is a major constituent of the atmosphere and it chemically bonds rapidly with nearly all solid materials that might be used as collectors. To overcome these two issues, a Solar Wind Concentrator was developed which focused ions onto a target to increase the fluence by a factor of ~ 20 (McComas et al. 1997; Nordholt et al. 2003), while at the same time rejecting hydrogen, which constitutes more than 95 % of the solar wind ions. Because it is impossible to accurately mimic the solar wind in a test chamber, a sophisticated computer model of the instrument was developed to predict its performance in concentrating the ions and to predict the instrumental fractionation of the ions collected in the target (Wiens et al. 2003). Instrumental fractionation, as the term is used here, refers to enhancement of one isotope or several isotopes in the Concentrator target, relative to these isotope ratios in the unconcentrated solar wind, such as an enhancement of ^{18}O relative to the unconcentrated solar wind $^{18}O/^{16}O$ ratio.

The performance of the Concentrator depended significantly on solar-wind charge state, angular distribution, and velocity distribution, even though the Concentrator's voltages were adjusted continuously as a function of velocity. As the distributions of some of these parameters vary over the 11-year solar cycle, and other parameters such as solar-wind angular distribution additionally involve the performance of the spacecraft pointing accuracy, the pre-flight models (Wiens et al. 2003) have been superseded by models using actual flight data. The post-flight results reported here are substantially different than pre-flight projections, and are of high importance to the science goals of the mission. The following section of this paper briefly reviews the Concentrator design. The next section describes the operation during flight and the condition of the targets after the capsule recovery. Following that is a description of the updated computer model of the instrument and the recent solar-wind parameters as experienced on board the spacecraft by the Concentrator. The Results section describes the outcomes of updated performance modeling, including many more cases than were originally undertaken (Wiens et al. 2003). The context of these results is discussed, giving reference to experimental work to verify the model results. We conclude with a discussion of (a) the similarities of the N, O, and Ne fractionation patterns, which are important to applying the Ne results of Heber et al. (2011) to unknown isotope ratios, and (b) simulations of other elements (e.g., D/H, C, Li, Mg, Si, S) of potential interest for using Concentrator targets and a discussion of the implications for analyses of new isotope ratios.

2 Instrument Description

The Concentrator is radially symmetric with a 41.6 cm diameter aperture at the entrance and a 40 cm diameter parabolic electrostatic mirror that focuses ions onto a target assembly 6.2 cm in diameter. Figure 1 shows a cross section of the electrostatic features of the instrument. The mirror used up to 10 kV potentials to reflect the ions back onto the target. The mirror was micro-stepped to act as a reverse Fresnel lens, reflecting the sunlight directly back into space instead of concentrating it on the target (Nordholt et al. 2003). Above the mirror electrode lines of equipotential were held in a parabolic shape by a domed grid positioned just above the electrode. A hydrogen rejection grid was employed to reduce proton-induced damage to the target assembly. An additional grid accelerated ions through a potential of 6.5 keV/q to straighten their trajectories, making it easier to uniformly focus ions incident at a range of angles and energies, and also to implant them farther into the target and reduce backscatter losses. The components maintained at −6.5 kV include the acceleration grid, target assembly, domed grid, and a cylindrical "accelerator can" around the perimeter (not shown in Fig. 1), which together formed a field-free cage at the center of the instrument, while the grounded grid at the top and the external shell of the instrument formed a grounded enclosure around the instrument.

The goal of the Concentrator was to enhance by an average factor of 20x the fluence of solar-wind oxygen ions of charge states +5 to +8 which constitutes ≫ 99 % of all solar-wind oxygen. The ideal would have been to obtain a homogeneous distribution of solar wind across the entire face of the target. A tightly focused beam does not give this result, so the beam is necessarily defocused. The degree of defocusing must take into account the angular distribution of the solar wind and the desires to avoid mass fractionation and maximize the concentration factor. The final design achieved its average of 20x concentration for the predicted solar-wind conditions with an acceptable predicted mass fractionation range for $^{18}O/^{16}O$ of approximately 25 permil (‰; parts per thousand relative to unconcentrated solar wind) in a relatively slowly varying radial pattern across the target (Wiens et al. 2003).

The Concentrator target assembly was designed to house several different collector materials, following the overall philosophy of exposing a variety of substrates which optimize the analyses of different elements in the solar wind (Jurewicz et al. 2003). The target assembly was thus made to house four quadrants of semiconductor material, one of which is shown in Fig. 2. The four quadrants were mounted facing towards the Concentrator's parabolic ion
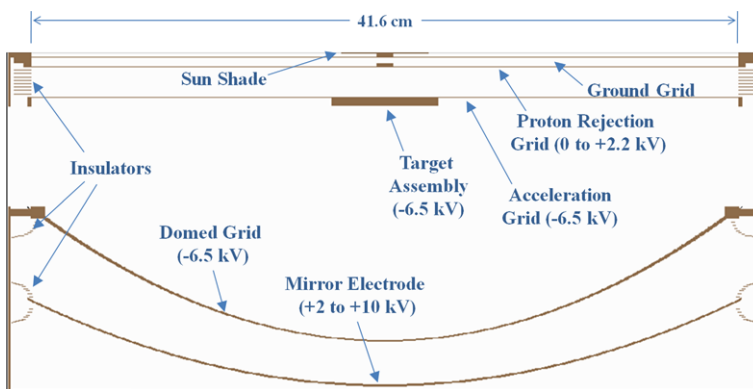

Fig. 1 Cross section of the Genesis mission Solar-Wind Concentrator instrument, taken from the SIMION model

Fig. 2 SiC target quadrant subsequent to disassembly after flight, shown with dimensions in English and metric units. *Light colored corners* were shielded by the gold cross support structure. The rest of the target was darkened by the exposure to solar wind
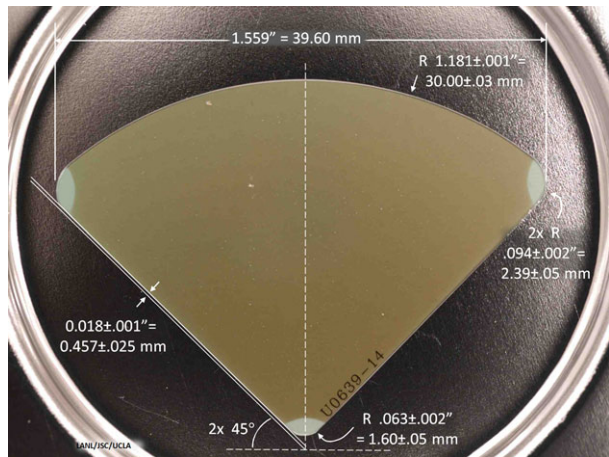
Fig. 3 The target assembly as it appeared during disassembly after landing. Dimensions of the gold cross and housing are given. The SiC quadrants are at 12-3 and 6-9 o'clock. The quadrant between them is ^{13}C diamond. The broken quadrant is diamond deposited on Si. A *small rectangle* of bare Si is visible just above and to the left of the center of the assembly. Dimensions are given in English and metric. Photo NASA JSC
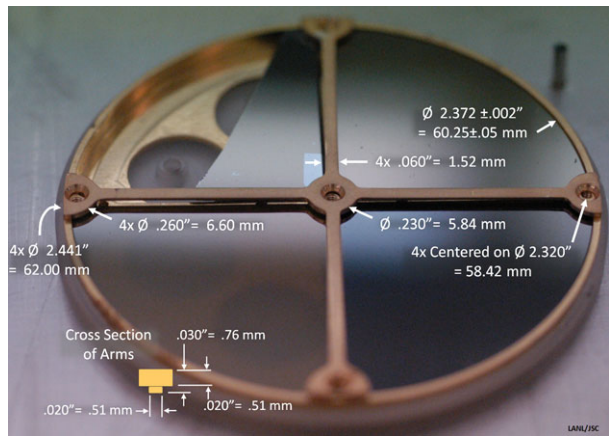
mirror and away from the Sun, in a holder centered on the axis of rotation of the instrument. The four quadrants were held in place by a gold-coated stainless-steel cross, the design of which is illustrated in Fig. 3.

The gold cross was designed as a structural support and was never intended for solar-wind analyses with the possible exception of neon. Nevertheless, it has been used for analyses (e.g., Heber et al. 2011; cf. Marty et al. 2010), prompting questions about its fabrication, described here. No special surface treatments were made to either the stainless steel or the gold to facilitate later analyses. The gold was electroplated on the stainless steel cross and the target housing at Los Alamos National Laboratory using a standard practice consisting of ultrasonicating with water and detergent, followed by a hot soak in NaOH and then a soak in HCl solution. A nickel strike was applied using NiCl solution electrolysis, and the gold was applied using KAuCN solution electrolysis. Gold-coated aluminum parts of the Concentrator were treated using a standard process consisting of a hot NaOH soak, a nitric-HF bath, sodium zincate, an electrode-less nickel coat provided by a nickel sulfate with sodium hypophosphite bath, and finally the KAuCN solution electrolysis. Pure water rinses were performed between every step and following the electrolysis. The Ni strike is typically ~ 1.2 μm on Al and less than that on stainless steel. The gold plate itself is 0.5–1.0 μm.

Witness plates and spare parts were coated with only the Ni strike or with the complete recipe. X-ray photo-electron spectroscopy (XPS) analyses indicated that traces of K could be found on the gold surfaces.

3 Instrument Operation in Flight

The Concentrator mirror electrode and H rejection grid voltages were adjusted every 30 s during flight, tracking the solar wind proton velocities determined onboard by the Genesis Ion Monitor (GIM; Barraclough et al. 2003). The mirror was kept at a multiple of 4.32 times the energy per charge at the peak of the proton distribution at all times except when it reached its maximum potential of 10 kV at a proton velocity of 667 km/s. Between this velocity and 800 km/s the mirror remained at 10 kV. The Concentrator was turned off on the rare occasions that the solar wind exceeded 800 km/s (3.35 kV/amu) to avoid driving any of the ions of interest into the mirror. The H rejection grid was kept at a potential between 1.0 and 1.3 times the energy per charge at the peak of the proton distribution. This factor was adjusted based on the temperature of the plasma, such that in hot plasma the H rejection voltage was turned down, or even off, to avoid rejecting any of the ions in the $m/q \geq 2.0$ range (Nordholt et al. 2003).

Because the voltages were commanded based on a running average of three GIM data cycles, the mean time lag between a measured solar wind speed and a Concentrator voltage change to match was approximately 1.5 GIM data cycles ($\sim$ 4 minutes), or around eight Concentrator data cycles. When comparing voltages of Concentrator 30 s data cycle numbers differing by eight, one finds that both the mirror and the H rejection grid experienced fractional voltage changes dV/V of ≤ 1 % fifty percent of the time. For the mirror electrode, dV/V reached the 90th percentile in occurrence for a 4 % change. It reached the 99th percentile for a 10 % change, and the 99.9th percentile for a 17 % change. The operation of the Concentrator mirror was designed with a 20 % margin in energy (i.e., would still focus ions with 20 % higher energy than the designed-for m/q range at any given instant), and it is clear that the Genesis payload and software were able to perform the integrated task of tracking the solar-wind speed and commanding the proper Concentrator response to easily meet that margin. Likewise, for the H rejection grid, the 90th percentile was reached at a dV/V of 7 %, the 99th percentile by 14 %, and the 99.9th percentile within a 24 % voltage difference. The H rejection grid operation was planned based on a more complicated function of both the solar-wind speed and temperature, based on mass fractionation calculations. As with the mirror electrode, the rate at which the H rejection grid tracked the solar wind velocity was well within its design margins.

Figure 4 shows the distribution of mirror and H rejection grid voltages during flight. Because the voltage did not track with the solar wind speed above 667 km/s, the mirror operated at 10 kV a larger fraction of the time than at any other voltage. Aside from this, the mirror voltage distribution peaked between 3 and 3.5 kV corresponding to the predominant low-speed solar wind. The H rejection grid pattern will be discussed in more detail below.

Overall, the instrument concentrated ions over 803.28 days between day 339 of 2001 and day 93 of 2004. The time intervals for the solar-wind Concentrator operation are given in Table S1 in the supporting online information. The Concentrator was turned off by the fault protection software four times due to a problem with the H rejection grid (described below), for a total of 26.05 days of non-operation. One of those times coincided with the spacecraft going into safe mode due to high-energy particles from a solar storm. The Concentrator was also turned off for each station-keeping maneuver (total of 6.42 days), for H rejection grid
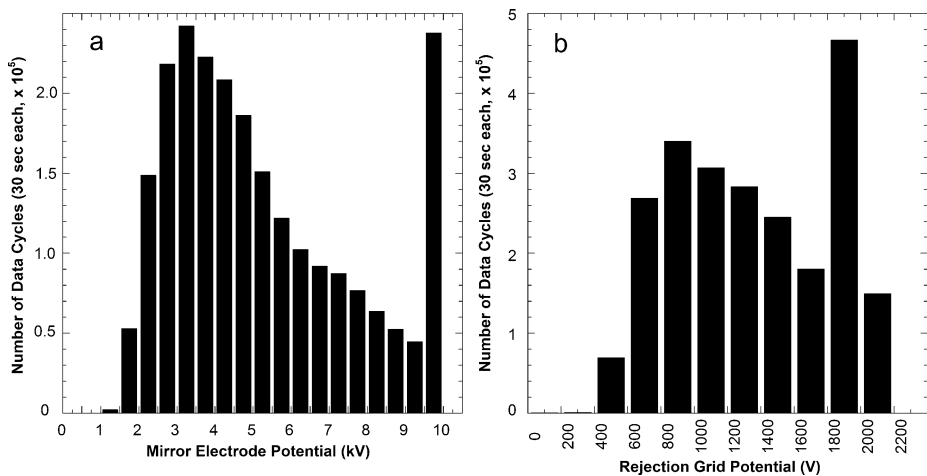
Fig. 4 Concentrator voltage distributions, for (**a**) the mirror and (**b**) the H rejection grid, during collection

tests (0.97 days) and any time GIM was not in autonomous mode or could not determine the solar-wind speed and temperature, such as during anomalously low density conditions (Barraclough et al. 2003). Additionally, the instrument autonomously turned itself to standby whenever the wind speed was consistently above 800 km/s (>600 km/s after 2004 day 54). In total, the instrument operated all but 44 days from the start of the Genesis mission science collection phase until its conclusion.

The H rejection grid was designed for a maximum potential of 3.5 kV. However, it encountered a problem during turn-on and could not be operated at its full potential. When a voltage was requested above which the grid was stable, the potential dropped to a constant level in the 1500–1700 V range and stayed there until a lower voltage was requested. It was observed that a higher voltage could be sustained if the grid potential was adjusted upwards in smaller increments. Software patches were uploaded that limited the voltage increments, and which also lowered the voltage and then returned it to normal if the H rejection grid potential dropped below the requested level. To avoid voltage drop-outs, a maximum potential was defined in software and was set slightly below the level at which the grid became unstable. Over the course of the mission the point of instability varied, apparently modulated by the instrument temperature, which was warmer near perihelia, during the winter months in the Earth's northern hemisphere. The software voltage limit was adjusted periodically to deal with this feature. The software limits used over the course of the collection period are shown in Fig. 5 and are given in Table S3 in the supporting online material. The voltage limitation explains the preponderance of 30 second intervals during which the H rejection grid was at 1.8–2.0 kV, shown in Fig. 4. Without this limitation the maximum incidence would have been at 0.8–1.0 kV, where a secondary peak can be seen. There was also a total of ∼ 200 minutes (0.017 % of operation time; too small to be seen in Fig. 4) during which the H rejection grid was turned off completely to avoid isotopic fractionation of heavy ions during periods of very high plasma temperature (Nordholt et al. 2003). During these intervals all ions including protons were accelerated towards the mirror and target.

Overall, the H rejection grid maximum voltage limitation is estimated to have increased the flow of hydrogen to the target by a factor of ∼ 2.5, with all of the additional hydrogen coming during high speed flows. This raised the maximum fluence to an estimated ∼ 1.5 × 10^{17} protons/cm^2 near the center of the target assembly.
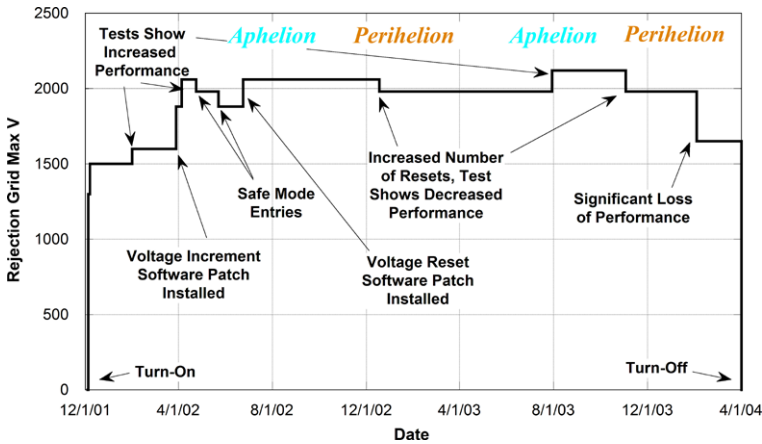
Fig. 5 Maximum Genesis Concentrator H Rejection Grid potential as a function of date

Fig. 6 The condition of the Concentrator as it was extricated and disassembled at the recovery site in Utah. The target assembly is facing away from the camera. Photo NASA JSC
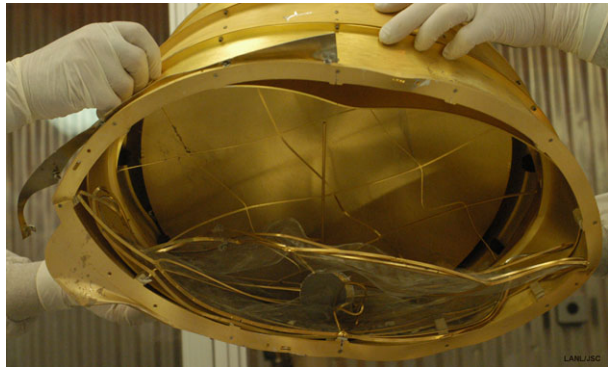
4 Post-Landing Conditions

The Concentrator targets were some of the very few semiconductor materials to survive the capsule's hard landing intact (Fig. 3), as the structure of the Concentrator, particularly the stainless steel grid and target supports, cushioned the impact. After the landing the target assembly was found near an interior wall of the Concentrator structure (Fig. 6). The quadrant closest to the wall, the diamond-like carbon-on-silicon (DOS) quadrant, was broken (Fig. 3), apparently from impact with the wall. Much of the material that had broken from that quadrant was recovered (Rodriguez et al. 2009). Even though the target was nested inside the Capsule, the Sample Canister, and the Concentrator, a couple of spots of Utah mud could be seen on the target assembly during disassembly. Additional characterization of surface contamination showed that >90 % of the particles are smaller than 5 μm, and most particles are from the capsule shell and ablator material (Calaway et al. 2008). Extensive photo documentation was made at high resolution by curation personnel for all four of the Concentrator quadrants (e.g., Allton et al. 2008; Calaway et al. 2008).

Prior to integration into the Genesis science canister the Concentrator grids had been carefully mapped to determine their exact positions, including any departures from the ideal shapes. The pre-flight position of the domed grid was used in all subsequent computer sim-

ulations of the instrument performance. Because this was the first solar-wind instrument to use this type of electrostatic grid (i.e., a woven design; Nordholt et al. 2003) and with the large aperture, there were significant concerns about thermal relaxation of the grids during flight. Thermal modeling indicated that the grids would achieve warmer temperatures than their frames, potentially leading to wrinkles and/or sagging. Additionally, the thermal mass of the grids was so miniscule that they would cool instantly upon being shaded during off-sun maneuvers. The mission plan thus called for the grids to be re-mapped after recovery, and, if the grids had relaxed significantly, for the instrument to be re-tested in a solar-wind simulation facility. The crash made it impossible to determine the amount of relaxation of the grids or to estimate their positions during flight. Fortunately, analyses of all four gold cross arms indicated complete radial symmetry during operation (Heber et al. 2011).

Genesis passive solar-wind collectors became coated during flight with a contaminant layer up to 15 nm thick (Burnett et al. 2005), although it is less than 5 nm on most samples. This material appears to be a polymerized organic, likely from the room-temperature vulcanizing (RTV) elastomeric sealant used on the array panel fasteners. The composition was measured by XPS to be 40–60 % C, 15–40 % O, 2–10 % F, 1–4 % N, and 4–20 % Si (Burnett et al. 2005; Calaway et al. 2006; cf. Schläppi et al. 2010). XPS analyses of one of the broken pieces of the DOS Concentrator target quadrant revealed a relatively thin layer of polymerized silicone and no detectable F (D. Burnett, personal communication). Ellipsometry measurements on SiC quadrant 60003 were modeled to suggest a surface film between 4 and 9 nm, though it is unclear if this effect was due to disordering from the radiation damage, which was much greater on the Concentrator targets than on the passive collectors, or if it was an actual contaminant layer (Calaway et al. 2007). In any case, the possible layer is well separated from the bulk of the implanted solar wind, which peaks at a depth of ~ 80 nm in the Concentrator targets.

Given the presence of contamination on the surfaces of Genesis collectors, it is critical that the ions implanted below the surface of the Concentrator target be unambiguously of solar wind origin (cf. Becker 2010). A very brief analysis is given here showing that contaminant ions are not credible as the major source of nitrogen or oxygen implanted in the Concentrator targets. During design and construction of the instrument great care was taken to avoid the possibility of contamination. All of the interior surfaces were coated with gold except for the grids, their supports, and the insulators. The gold-coated surfaces appeared mostly clean upon return, consistent with the fact that most of them were at relatively high temperatures (estimated between 150 and 350 °C) during collection due to the low emissivity of gold. Contaminants are not likely to condense on surfaces at these temperatures. The insulators were recessed wherever possible, so that a minimum of ions would impinge on them. Insulator surfaces likely to still be exposed to ions were coated with SiC doped with ppm levels of nitrogen to provide enough conductivity to bleed any current induced by incident ions while being resistive enough to not overload the power supplies (Nordholt et al. 2003). The electrostatic grids were not gold coated so as to maximize their transparency (90.44 % each; Nordholt et al. 2003) and also to avoid increasing their temperature during exposure to sunlight. Because they were not gold-coated, the stainless-steel grids are considered to be the main potential source of any oxygen (or nitrogen) contaminant implanted in the target.

Only particles sputtered from the grids under specialized conditions could have possibly produced contamination in the target. Neutral species would not have been implanted into the target; only ions that were accelerated by the 6.5 kV potential could have been driven into the interior. Because of their different potentials, not all grids could contribute contaminant ions to the target. Any low-energy ions produced by sputtering of the ground grid would

be ejected from the instrument by the positive potential of the neighboring H rejection grid (Fig. 1). Low energy ions sputtered from the acceleration grid and domed grid would also not be implanted, as they have the same potential as the target. Low-energy ions sputtered into the interior of the Concentrator from the H rejection grid are the only ones that would be accelerated and implanted into the target. The flux of solar-wind ions striking the H rejection grid is relatively low, as ~ 80 % of the protons are rejected by the positive potential before they arrive at the grid. The H rejection grid fractional cross section is 0.0966 for heavy ions and might be slightly higher (e.g., conservatively ~ 0.2) for protons that were slowed but not reflected, as these particles may be traveling at a shallower angle relative to the grid. Given an average solar wind flux of $\sim 3 \times 10^8$ protons/cm^2/s, 1×10^7 alpha particles/cm^2/s, and 2.5×10^5 heavier ions/cm^2/s, with a mean neutral sputter yield of $< 1 \times 10^{-4}$ for low-energy protons (with only a small fraction of their original energy), ~ 0.1 for alpha particles around 2 keV, and ~ 1 for heavy ions, approximately 1×10^3 cm^{-2} s^{-1} each, of proton-induced and alpha-induced neutrals, and $\sim 2 \times 10^4$ cm^{-2} s^{-1} heavy ion-induced neutrals would be produced. Relative to the neutral sputtering yield, the ion sputtering yield is at most 1 % for the high ionization potentials of O and N considered here. A worst-case approximation would consider the surface of the grid to be pure FeO (50 % oxygen), yielding an upper limit of ~ 500 O$^+$cm^{-2} s^{-1} of contamination impinging on the target. This compares with $\sim 2 \times 10^5$ cm^{-2} s^{-1} solar wind oxygen ions, giving an upper limit of oxygen contamination of ~ 0.25 %. For nitrogen one might assume a maximum of 10 % of the species sputtered from the grids are nitrogen which, compared to the solar-wind nitrogen flux, gives a maximum of 0.5 % contamination, but is likely orders of magnitude lower.

To address the potential for radiation damage in the Concentrator targets, test samples of target materials were implanted with H at the expected solar wind fluence along with ^{18}O and ^{15}N in the 10^{14} cm^{-2} range. To simulate the solar wind energy distribution the H was implanted at three different energies in differing amounts: 50 % at 20 keV, 30 % at 17 keV, and 20 % at 14 keV, all implanted as H$_3^+$, which is easily produced in the plasma source, with fluences up to 2×10^{17} cm^{-2}. The test samples included SiC from CREE that were identical to those in the instrument. These samples were heated to various temperatures between 300 and 600 °C for times ranging from one to six months. Secondary ion mass spectrometry (SIMS) analyses showed no detectable changes in the implant depth distributions of ^{18}O and ^{15}N, although considerable broadening of the H depth profiles occurred (D.S. Burnett, unpublished data). In addition, a set of H-, ^{18}O-, and ^{15}N-implanted Concentrator target materials were heated in vacuum at the nominal flight temperature (160 °C) for 27 months. These long-term implant samples provide controls accurately simulating of the flight thermal history. SIMS analyses of these showed no detectable perturbations to the ^{18}O and ^{15}N implant depth distributions.

Numerous analyses of the SiC targets themselves confirm that increased hydrogen fluence has not prevented any of the Concentrator analyses to date (Marty et al. 2010, 2011; McKeegan et al. 2011; Kallio et al. 2010; Heber et al. 2011). However, high-resolution imaging of the diamond-on-silicon target, which has not been analyzed for implanted material yet, shows widespread blistering on the center half of the target, apparently due to radiation (J. Allton, personal communication).

5 Ion Modeling

In this section we describe the ion optical modeling that was performed subsequent to the launch of Genesis, with a view to describing and discussing in this and following sections the

differences from pre-launch projections, comparisons with measurements on some elements, and projections for what to expect on other elements yet to be analyzed.

## 5.1 Differences between Pre-Flight and Post-Flight Modeling

Extensive ion optical modeling of the instrument was done in the design phase and prior to flight (Wiens et al. 2003) using the SIMION 7.0 package (Dahl 2000). The ion-optical model used an array of 23 million grid points to simulate the structure and interior of the instrument to a geometrical resolution of 0.67 mm. The model assumed completely flat ground, H rejection, and acceleration grids, but it incorporated a map of the pre-launch shape of the domed grid. All of the grids were modeled as equipotential surfaces, as the grid wires are much too small to model geometrically. Because the Concentrator operated at different voltages depending on the solar wind speed, the model simulated solar wind proton speeds at 100 km/s intervals between 350 and 750 km/s. For each of these five cases, approximately one million ions of each isotope were flown, initialized by sampling solar wind angle and charge-state distributions. As a large fraction of the ions impacted the target at relatively high angles, a backscattering simulation feature was incorporated based on both energy and angle of the ions, using statistical results from the Stopping and Ranges of Ions in Matter (SRIM) code (Ziegler et al. 2010). Simulations were done for ^{20,22}Ne, ^{16,18}O, ^{4}He, and H prior to flight, using the latter two species to determine the nature of possible radiation damage to the target. The model was used to optimize the acceleration voltage and to check for radial asymmetry and other idiosyncrasies, as well as to predict the overall concentration of species and isotopic fractionation as a function of radial position on the target. For the latter two parameters, the model yielded only the radial position of each ion impact. The results showed that the Concentrator just met its requirement for an average concentration factor of 20x, though the enhancement was strongly peaked, achieving a factor of over 50x near the center, with an enhancement of less than 10x near the edge. The instrumental isotopic fractionation predicted for ^{18}O/^{16}O was confined to a range of just under 25 permil with an ^{18}O/^{16}O minimum at a target radius between 15 and 20 mm (Wiens et al. 2003).

More recently the model was improved, facilitated by migrating to SIMION 8.0 on newer computers. The new model has a resolution of 0.40 mm and uses 110 million grid points to simulate one quadrant of the instrument (and the rest by symmetry). The new resolution represents a 40 % decrease in inter-grid-point distance, and the new model uses more than four times the number of grid points as previously. As in the first model, the field-free region between the acceleration grid and the domed grid is modeled simply by free space. Extensive checking was done against the as-built drawings to ensure that the model accurately reproduces the flight instrument. The input program used to fly the ions remains largely unchanged except for the revised input parameters described below.

As mentioned above, the H rejection grid potential was unexpectedly limited during flight. In post-flight modeling the H rejection grid potential was set 10 % above the kinetic energy of the protons, e.g., $1.1 * (0.5 * m_p * v_p^2)$ for the lower three velocity bins (300–400, 400–500, and 500–600 km/s). For the highest two velocity bins it was set at 1900 V, which is near the maximum potential allowed during the mission (Fig. 5). These settings should have essentially no effect on the ion modeling, as no ions with $m/q < 1.5$ are discussed here.

The parameters used to simulate ion backscattering at the target were improved significantly. Ions were run in SRIM at 5° intervals from 0 to 60°, and over an energy range representative of all ions at the target, in up to twelve different energy bins for each angle. For oxygen and neon, 75,000 ions were run per bin, totaling ~ 50 million ions in over 600 runs. The results were fit by using a 3D minimization technique. Backscatter modeling and

Fig. 7 Comparison of pre-flight
velocity distribution projections
and the oxygen velocity
distribution ("O Dist") obtained
by the ACE SWICS instrument
during the Genesis solar-wind
collection
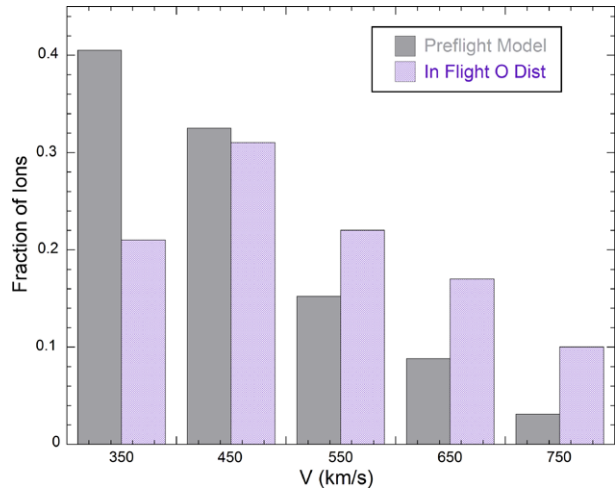
fitting of He, Li, N, Mg, and Ar into SiC, and C into Si, were done on a similar scale to the
O and Ne calculations. In all cases the results were fit by an empirical equation

$$b = x - y\bigl(\log(E)\bigr) \tag{1}$$

where b = percent backscattered, x and y are fourth-order polynomials of the angle in de-
grees, and E is the incident ion energy in KeV. The fitted coefficients of x and y are given
in Table S4 in the supporting online material. Argon had a maximum backscatter of <5 %
at 60 deg. The maximum backscatter for O was ~ 8 % under the same conditions, while
He backscattering was up to ~ 15 %. Backscattering was not modeled for Si or S because
their backscatter fraction is very low relative to the poorer accuracy of the modeling results
for these elements, as discussed later. The backscattering correction was done for the other
elements as part of the Monte Carlo simulation program that flies ions into the Concen-
trator. Ions that backscattered in the simulation were simply excluded from the resulting
distribution of ions in the target.

5.2 Solar Wind Conditions During Flight

Prior to flight the best estimates of various solar-wind parameters such as velocity, angular
distribution, and charge state distribution were used in the pre-flight modeling (Wiens et al.
2003). As will be shown below, small changes in these parameters, particularly for velocity
and angular distribution, have a major effect on the performance of the instrument. Because
of this, it was important to catalogue the in-flight conditions (e.g., Reisenfeld et al. 2012)
and to revise the parameters by using actual flight data.

The velocity distribution of solar-wind ions has a significant effect on the overall outcome
of the Concentrator performance in terms of both isotopic fractionation and concentration.
The fraction of ions hitting the target drops from 85 to 65 % between 350 and 650 km/s
(see supporting online material). The ability of the -6.5 kV acceleration grid to straighten
the trajectories of higher velocity ions is reduced, and these ions are focused less efficiently
onto the target. Figure 7 shows a comparison between the pre-flight estimate and the in-
flight data for oxygen, measured by ACE SWICS during the Concentrator operation times.
As discussed in Reisenfeld et al. (2012), Genesis encountered significantly more high-speed
wind than expected for a long-term average, in part due to the recurrence of a high-speed

Fig. 8 Comparison of the pre-flight expected angular distribution for ions entering the Concentrator (*lower curve*) and flight data from the Genesis ion monitor (*upper curves with symbols* indicating velocity bins)
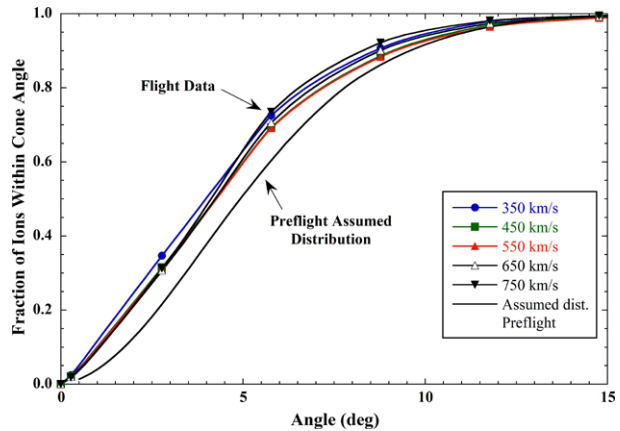
stream at each solar rotation over several months. Figure 7 shows that the <400 km/s bin contained only about half as large a proportion as expected, resulting in a 5 % lower overall concentration, with that of oxygen dropping from a target-averaged value of 20.7 to 19.7. The target-averaged oxygen isotopic composition also becomes heavier by nearly 2.5 ‰ in $\delta^{18}O$ as more of the ^{16}O misses the target than do the heavier isotopes. (Units used here indicate deviations in the abundance of the isotope in question, here ^{18}O, relative to the major isotope, which for oxygen is ^{16}O.)

Along with the velocities, the angular distribution of incoming solar wind ions strongly affects performance. The angular distribution includes both the instantaneous average velocity vector relative to the instrument and also the angular spread due to the thermal broadening of the distribution, and these were convolved together for pre-flight angle estimates (Wiens et al. 2003). Here we discuss the best estimate of the angular distribution of solar-wind ions during the collection period based on our knowledge of the actual spacecraft orientation and the flight solar wind conditions based on GIM data.

The apparent angular distribution is affected by the spacecraft's pointing capabilities. Genesis had autonomous daily one-degree corrections to keep it pointed into the solar wind. As a spin-stabilized platform, it experienced some nutation as a result of each correction. Misalignment of the spin axis and center of mass may have resulted in small amounts of wobble during portions of the mission as well. The Genesis spin axis was maintained an average of 4.5° ahead of the Sun to compensate for the effect of the forward motion of the spacecraft. This minimized the average angle between the solar wind flow direction and the spin axis (and the Concentrator bore-sight).

To determine the solar-wind ion angular distribution experienced by the Concentrator, its boresight and the axis of rotation for GIM are considered to be coincident. With this assumption we can use the eight GIM channels to determine the solar wind angular distribution experienced by the Concentrator. The result averaged over the Concentrator collection period is shown for protons in Fig. 8 with separate curves for different velocity bins. Also shown is the angular distribution assumed for Concentrator performance calculations prior to flight. The pre-flight angular distribution was taken from OMNI 2 data (King and Papitashvili 2005) convolved with expected worst-case Genesis spacecraft pointing performance. The actual pointing performance was clearly better than expected.

Finally, charge state distributions were revisited for the relevant ions. Carbon, O, Ne, Mg, and Si distributions used in post-flight simulations utilized Advanced Composition Explorer (ACE) Solar Wind Ion Composition Spectrometer (SWICS; Gloeckler et al. 1998)

Table 1 C, N, O, Ne, Mg, and Si charge state distributions obtained from ACE/SWICS (Gloeckler et al. 1998) data over the Concentrator operation period, used in post-flight simulations. Mean charge state and mass per charge is also noted

Element	< 400 km/s	400–500 km/s	500–600 km/s	600–700 km/s	700–800 km/s	m/q[a]
C^{+4}	0.17	0.16	0.19	0.22	0.24	3.3
C^{+5}	0.41	0.41	0.44	0.51	0.54	2.6
C^{+6}	0.42	0.43	0.37	0.27	0.21	2.2
C mean	**5.25**	**5.26**	**5.18**	**5.05**	**4.97**	**2.6**
N^{+4}	0.01	0.01	0.01	0.01	0.01	3.8
N^{+5}	0.96	0.96	0.96	0.96	0.96	3.0
N^{+6}	0.03	0.03	0.03	0.03	0.03	2.5
N mean	**5.08**	**5.08**	**5.08**	**5.08**	**5.08**	**3.0**
O^{+5}	0.02	0.02	0.02	0.02	0.02	3.6
O^{+6}	0.72	0.79	0.87	0.92	0.94	3.0
O^{+7}	0.24	0.17	0.10	0.06	0.04	2.6
O^{+8}	0.02	0.02	0.01	0.003	0.004	2.3
O mean	**6.26**	**6.19**	**6.11**	**6.05**	**6.03**	**3.0**
Ne^{+6}	0.08	0.09	0.11	0.11	0.09	3.7
Ne^{+7}	0.24	0.24	0.26	0.23	0.23	3.1
Ne^{+8}	0.65	0.65	0.62	0.65	0.67	2.8
Ne^{+9}	0.03	0.02	0.01	0.007	0.005	2.4
Ne mean	**7.63**	**7.60**	**7.54**	**7.55**	**7.59**	**2.9**
Mg^{+6}	0.07	0.08	0.08	0.05	0.06	4.3
Mg^{+7}	0.03	0.03	0.05	0.07	0.10	3.7
Mg^{+8}	0.09	0.09	0.12	0.18	0.21	3.3
Mg^{+9}	0.31	0.31	0.33	0.36	0.37	2.9
Mg^{+10}	0.50	0.48	0.41	0.33	0.25	2.6
Mg^{+11}	0.001	0.001	0.000	0.000	0.000	2.4
Mg mean	**9.13**	**9.09**	**8.96**	**8.85**	**8.67**	**2.9**
Si^{+6}	0.05	0.04	0.04	0.03	0.03	5.0
Si^{+7}	0.16	0.15	0.17	0.18	0.18	4.3
Si^{+8}	0.26	0.25	0.27	0.29	0.30	3.8
Si^{+9}	0.28	0.28	0.28	0.30	0.31	3.3
Si^{+10}	0.14	0.15	0.15	0.14	0.14	3.0
Si^{+11}	0.05	0.06	0.04	0.03	0.02	2.7
Si^{+12}	0.06	0.06	0.05	0.03	0.03	2.5
Si mean	**8.70**	**8.78**	**8.65**	**8.54**	**8.52**	**3.5**

[a]The m/q column uses the mass of the heaviest isotope. The mean m/q (bold) uses the lowest mean charge

data averaged over the complete Concentrator operation time period, given in Table 1. Oxygen distributions are more peaked at +6 (i.e., have slightly lower average charge overall) than those used in pre-flight simulations (Wiens et al. 2003), with the exception of the 700–800 km/s bin, in which the former data relied on Ulysses distributions. Charge states used in recent modeling for nitrogen (Table 1) are from Gloeckler and Geiss (2007), which in reality represents fast polar coronal solar wind, but is here used for all speeds because a represen-

Table 2 Charge state distributions of Ar, S, Si, Mg, C, and N as functions of freeze-in temperature

Element	Charge St	Frequency			m/q[a]
		1.0 MK	1.2 MK	1.5 MK	
Ar	7	0.018	0.010	0.003	5.4
Ar	8	0.712	0.509	0.245	4.8
Ar	9	0.247	0.389	0.434	4.2
Ar	10	0.021	0.086	0.261	3.8
Ar	11	0.0004	0.006	0.053	3.5
Ar	**mean**	**8.27**	**8.56**	**9.13**	**4.4**
S	6	0.075	0.021	0.003	5.7
S	7	0.365	0.185	0.05	4.9
S	8	0.426	0.435	0.251	4.3
S	9	0.124	0.29	0.402	3.8
S	10	0.011	0.063	0.236	3.4
S	11	0.0002	0.004	0.053	3.1
S	**mean**	**7.62**	**8.2**	**9**	**4.1**
Si	6	0.090	0.025	0.003	5.0
Si	7	0.368	0.185	0.042	4.3
Si	8	0.397	0.403	0.194	3.8
Si	9	0.128	0.297	0.345	3.3
Si	10	0.013	0.079	0.269	3.0
Si	11	0.0005	0.009	0.095	2.7
Si	12	2.0E–05	0.001	0.052	2.5
Si	**mean**	**7.59**	**8.25**	**9.33**	**3.6**
Mg	6	0.064	0.009	0.0005	4.3
Mg	7	0.247	0.066	0.007	3.7
Mg	8	0.353	0.200	0.051	3.3
Mg	9	0.177	0.230	0.143	2.9
Mg	10	0.155	0.494	0.798	2.6
Mg	**mean**	**8.07**	**9.13**	**9.73**	**2.8**
C	4	0.269	0.116	0.031	3.3
C	5	0.584	0.494	0.265	2.6
C	6	0.148	0.390	0.704	2.2
C	**mean**	**4.88**	**5.27**	**5.67**	**2.5**
N	5	0.847	0.646	0.348	3.0
N	6	0.150	0.335	0.519	2.5
N	7	0.002	0.018	0.133	2.1
N	**mean**	**5.15**	**5.37**	**5.79**	**2.8**

[a]The m/q column uses the mass of the heaviest isotope. The mean m/q uses the 1.2 MK mean charge

tative charge state distribution for slow wind could not be found. Helium was assumed to be completely ionized. Distributions for Li, C, N, Mg, Si, S, and Ar were calculated based on coronal freeze-in temperatures of 1.0, 1.2, and 1.5 MK using the recombination rates of Bryans et al. (2006), and all but Li are given in Table 2. More than 99.9 % of all Li is calculated to be +3. Charge state distributions corresponding to 1.2 MK were used for the S and Ar simulations.

Carbon, Mg, and Si charge data are included in both Tables 1 and 2 as a check on the robustness of applying 1.2 MK for the above elements. Comparing the weighted mean charge states of these elements in Table 1 one sees that the ACE data corresponds very closely to 1.2 MK (Table 2) for velocities lower than 500 km/s, but higher velocity bins tend toward a lower mean charge. However, the higher velocity charge states are still closest to the mean charges corresponding to 1.2 MK (Table 2). For this reason, charge states corresponding to 1.2 MK were used for all velocity runs for S and Ar. A more comprehensive empirical treatment of freeze-in temperatures as a function of solar-wind velocity is compiled in Wurz (2001). In hindsight, for nitrogen, the charge state distribution calculated from the freeze-in temperature of 1.2 MK should probably have been used rather than Ulysses data. Comparison of nitrogen in Tables 1 and 2 show the 1.2 MK distribution to include a significant fraction (34 %) of the +6 charge state, while the coronal hole data used consists of almost entirely +5. However, it can be argued that the coronal hole distribution is more likely to produce an anomalous result, which was not observed.

6 Results

Tables 3 and 4 give the model concentration factors and isotopic fractionations, respectively, relative to the normal solar wind, as functions of the target radius for 5 mm radial bins for all of the elements discussed below. The mean values given at the right side of the tables were determined from the sums of all ions hitting the target, using a target radius of 31 mm when the structure is included (Fig. 3). Table 4 and figures in the remainder of this paper use a delta (δ) notation which gives the deviations of the ratio of the specified heavy isotope to the lightest isotope in permil relative to unconcentrated solar wind. The next section

Table 3 Predicted concentration factors for radial bins of the target

	0–5 mm	5–10 mm	10–15 mm	15–20 mm	20–25 mm	25–30 mm	Ave.
^{4}He	50	46	35	23	13	6.4	19.2
^{6}Li	51	46	36	23	13	6.5	19.3
^{12}C in Si	53	48	36	23	12	6.4	19.4
^{14}N	57	51	38	23	12	6.4	19.6
^{16}O	56	50	38	23	13	6.5	19.7
^{16}O no Alfven[a]	55	50	38	24	13	6.6	19.7
^{16}O bowed grid[a]	57	51	38	24	13	6.6	19.8
^{16}O Gaussian[a]	56	50	38	23	13	6.5	19.7
^{16}O +8 only[a]	55	50	38	24	13	6.6	19.8
^{20}Ne	58	52	38	24	13	6.4	19.9
^{24}Mg	57	51	38	23	13	6.5	19.7
^{28}Si[b]	58	51	37	23	12	6.4	19.6
^{32}S[b]	55	48	34	20	11	5.7	18.6
^{36}Ar	52	45	31	18	10	5.2	17.9

Unless otherwise stated, the target is SiC

[a]Special cases for oxygen are described in the text. "Alfven" refers to differential heavy ion streaming

[b]Backscattering was not included, as its effect is relatively small for heavy ions

Table 4 Predicted isotopic fractionations in permil for radial bins of the target

	0–5 mm	5–10 mm	10–15 mm	15–20 mm	20–25 mm	25–30 mm	Ave.	Unc.
δ^4He	69	51	29	−21	−49	−41	2.9	0.6
δ^7Li	40	30	15	−13	−22	−19	3.8	0.8
δ^{13}C in Si	19	14	4	−13	−15	−10	−1.0	0.6
δ^{15}N	16	15	1	−10	−3	−2	1.6	0.6
δ^{18}O	34	20	2	−15	−9	−4	1.9	0.6
δ^{18}O no Alfven[a]	33	22	8	−14	−13	−13	2.0	0.6
δ^{18}O bowed grid[a]	29	24	2	−15	−14	−9	1.3	0.6
δ^{18}O Gaussian[a]	22	21	2	−17	−16	−1	0.0	1.0
δ^{18}O +8 only[a]	35	19	6	−13	−10	−7	2.5	0.6
δ^{22}Ne	28	14	−1	−13	−10	−8	−0.6	0.6
δ^{21}Ne	16	7	−1	−6	−5	−5	−0.4	0.6
δ^{26}Mg	8	−1	−17	−27	−26	−21	−15.7	0.6
δ^{30}Si[b]	−4	−5	−19	−26	−29	−18	−18.0	0.8
δ^{34}S[b]	−14	−38	−45	−55	−53	−47	−44.6	1.2
δ^{38}Ar	−43	−51	−73	−77	−77	−68	−66.7	0.9

Isotopic fractionation is given in parts per thousand (permil) deviations from unconcentrated solar wind; the heavy isotope is ratioed to the lightest stable isotope of each element. Unless otherwise stated, the target is SiC. Statistical uncertainty of each radial bin is in the range of ±1.3 ‰ for central bins to ±2.5 ‰ for innermost and outermost bins. Calculations assume a uniform SW isotopic composition as a function of velocity (see text)

[a]Special cases for oxygen are described in the text. "Alfven" refers to differential heavy ion streaming

[b]Backscattering was not included, as its effect is relatively small for heavy ions

Fig. 9 Comparison of pre-flight and post-flight instrumental fractionation simulations for oxygen implanted into SiC targets. Each data point represents the mean of a 5 mm radial strip. *Error bars* represent statistical uncertainties of the model results. *Dashed lines* connect the data points. The delta values plotted on the *y*-axis are relative to unfractionated solar wind
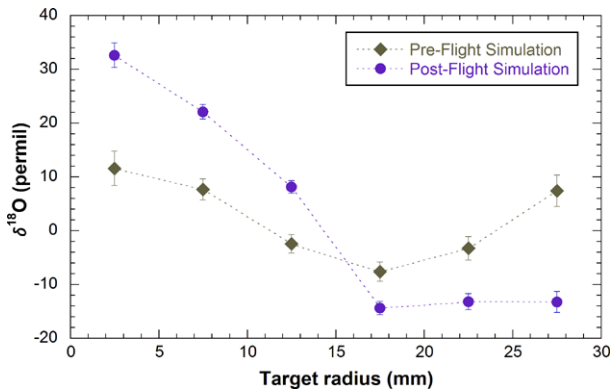
compares pre- and post-flight simulations and measured versus model results. Following that the results of some variations on the basic model are given, and finally, calculations for He and Ar concentration are compared with measured results.

Fig. 10 Neon measured (Heber et al. 2011) and simulated. As in Fig. 9, each simulation data point represents a 5 mm mean
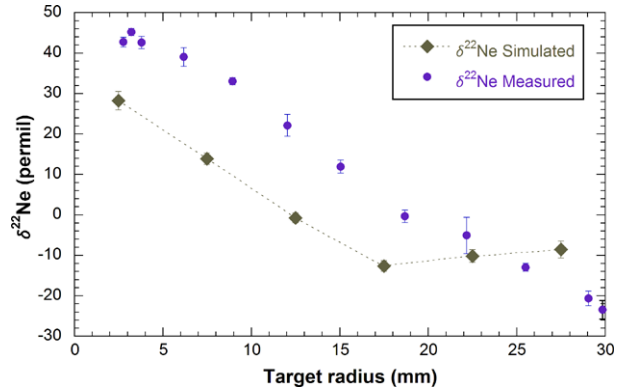
6.1 Comparisons of Oxygen and Neon Between Pre- and Post-Flight Simulations and Measured

Figure 9 shows a comparison between pre-flight and post-flight modeling of the instrument fractionation as a function of the radial position on the target for $^{18}O/^{16}O$. As in Tables 3 and 4, each model data point in Fig. 9 represents a 5 mm radial bin. Simulation conditions are the same except the post-flight version used SIMION 8.0 with the higher resolution ion-optical model of the Concentrator compared to the SIMION 7.0 model. Also, the velocities, angular distributions, and charge state distributions were revised as noted.

The pre- and post-flight simulations are clearly different, with the post-flight simulation showing an isotopic fractionation range approximately twice that of the pre-flight simulation. Both curves show enrichment of ^{18}O near the center of the target, then a drop to a low point in the 15–20 mm radial bin, and then a rise or leveling off toward the outer edge of the target. The difference is for the most part not due to changes in the model, as SIMION 7.0 and 8.0 model results were almost statistically indistinguishable when run with the same input conditions. Rather, the increasing steepness of the trend from the center is due to the tighter angular distribution used in the post-flight simulation. In the extreme case of a parallel beam better focusing is obtained for the heavier ion due to its greater momentum, which causes it to reflect closer to the solid mirror electrode surface, while the lighter ion reflects closer to the domed grid. This grid is stretched across a support structure that forms part of a paraboloid of revolution, but because the grid, under tension, minimizes the distance between supports, the resulting surface has a distinct waffle pattern to it (cf. Fig. 6). The result is poorer focusing of the lighter ion, and significant fractionation in the case of a very tight angular distribution. In the instrument design, this was balanced against the accelerating potential, which acted to control the angular distribution of the ions as they approached the mirror (Nordholt et al. 2003). The pre-flight design was optimized for an accelerating voltage of −6.5 kV, given the estimated angular distribution. If the post-flight angular distribution had been anticipated, a slightly lower accelerating potential would have been used to minimize fractionation.

Figure 10 shows experimentally measured versus post-flight modeled isotopic fractionation for $^{22}Ne/^{20}Ne$. There are no independent measurements, at this precision, of the isotopic composition of unconcentrated solar wind oxygen, the element of greatest interest, so it is not possible to experimentally determine the instrument fractionation for that element. However, the solar wind neon isotopic composition was measured both unconcentrated (e.g., Heber et al. 2009) and in the Concentrator targets, providing a determination of the instrumental fractionation for that element. We therefore use neon (Heber et al. 2011) for the

comparison in Fig. 10. The measured data are parallel to the simulated data from zero to twenty mm radius, but instead of turning over or leveling off as the simulation predicts, the measured data continue with nearly the same slope all the way to the outer edge of the target. The difference near the outer edge of the target will be discussed later. Not counting the measured data point closest to the center of the target (left edge in Fig. 10), which was in the shadow of the target frame (Figs. 2 and 3), the slopes of the simulated and measured data from 0 to 20 mm radius are within three percent of each other, well within uncertainty of being identical. Note however, the measured fractionation is consistently 20 permil greater than the simulated fractionation in this region.

An important distinction is made between mass-dependent and mass-independent fractionation of isotopes, as very different processes in nature are invoked in the two cases. Mass-dependent fractionation affects different isotope ratios of the same element based on the relative mass differences of the isotopes. For example, a mass-dependent effect will be approximately twice as strong on $^{18}O/^{16}O$ as on $^{17}O/^{16}O$, with slight second-order differences in mass-dependent effects depending on whether the effect is kinetic or an equilibrium reaction (e.g., Young et al. 2002). Most of the modeling was done comparing only two isotopes of each element. However, to ensure that the instrumental fractionation is mass dependent, all three isotopes were run for neon, and the velocity-averaged results are given in Table 4. Each radial bin is within uncertainty of mass-dependent fractionation. The different velocity bins all follow a mass-dependent fractionation except for the highest-velocity bin (700–800 km/s), where the fractionation per amu of $^{22}Ne/^{20}Ne$ was significantly stronger than that of $^{21}Ne/^{20}Ne$. However, the wind in this high-velocity bin did not contribute much to the total, and so the velocity-averaged neon is well within uncertainties of a mass-dependent fractionation overall, consistent with the measurements of Heber et al. (2011). The full neon results and uncertainties are given in Table S6 in the supporting online material. The effect of the high-velocity bin to the overall modeling will be discussed later.

6.2 Modeling Variations

Additional features were tested to potentially make the model more realistic. One aspect was to increase the speed of the ions to account for differential ion-proton streaming. It is observed that the outflow speed of helium and other heavy ions is usually higher than the proton speed (e.g., Marsch et al. 1982; Hefti et al. 1998). This differential streaming is a result of the Alfvén waves carried by the protons pushing the minor ions outward at a significant fraction of the Alfvén speed, V_A (~ 65 km/s on average at 1 AU). The streaming is limited to a fraction of V_A by plasma instabilities in such a manner that ions stream at a greater fraction of V_A as the proton speed increases. To investigate this effect on the model, instead of running the model at 100 km/s intervals between 350–750 km/s, ions were flown with mean velocities of 368, 475, 580, 686, and 790 km/s while the voltages were set to match proton speeds of 350, 450, 550, 650, and 750 km/s. These speeds are based on ACE/SWICS observations of alpha particle differential streaming in the solar wind during the Genesis collection period. This feature appeared to result in only a slight difference in the outer radial bin for oxygen, as shown in Fig. 11 by a comparison of instrumental fractionation curves with and without the differential streaming correction, though it did make a more substantial difference for Ar, as will be discussed in a later section.

One may also question whether differences in the average direction of streaming between protons and heavy ions have a significant effect on the Concentrator results. An analysis of the angular deviation from the radial direction was carried out for protons and alpha particles

Fig. 11 Comparison of oxygen simulations with different features described in the text
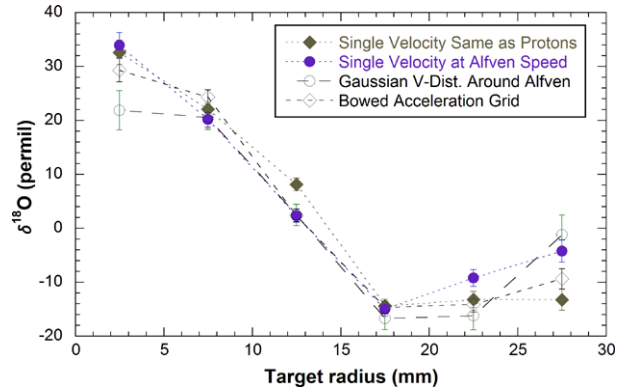

based on their temperature spread and the variation in bulk flow direction. For protons the thermal broadening gives a mean angular deviation of 4.9° and a flow variation of 3.3° from radial, resulting in an rms mean of 5.9°. By comparison, alpha particles showed a 4.0° deviation from thermal broadening and 2.8° in flow variation for an rms mean of 4.9°. The other heavy ion species studied here should behave similarly to the alphas, and so we conclude that the mean of the angular spread we used (Fig. 8) should be within one degree of the actual spread, with the modeled spread being slightly wider. This is consistent with the neon results in Fig. 10, and of the He and Ar results given below, which, if anything, imply a very slightly narrower spread.

Another feature to be tested was a Gaussian velocity distribution. The angular distribution including the transverse thermal distribution was already modeled, so only the velocities along the mean flow direction needed to be modified. The following full-width half max (FWHM) velocity dispersions were calculated from ACE/SWICS observations of the He, O, and Fe temperatures during the Genesis collection period and tested with each respective velocity bin at ∼ 100 km/s intervals from 350–750 km/s: 20.7, 29.4, 38.8, 54, 68.6 km/s. When used along with the differential streaming correction the instrumental fractionation curve for oxygen was almost identical to the non-Gaussian simulation (Fig. 11), but with a statistically significant reduction in fractionation in the first bin. As will be discussed later the combination of both Alfven velocity and Gaussian features did not appear to fit the argon fractionation pattern.

A final feature to be tested was to modify the shape of the flat grids. As mentioned earlier, these grids were very susceptible to thermal stresses, and because of the condition of the Concentrator after the hard landing it was impossible to determine if these grids had become loose in flight. Thermal models of the Concentrator suggested that these grids could have become significantly warmer than the bulk of the instrument. The grids and their support frames were both made of stainless steel so their thermal coefficients of expansion matched. However, the geometry of the fine grid wires may have resulted in higher temperatures. To check for this possibility, a worst-case thermal difference of 150° C was assumed, and using a typical linear expansion rate for stainless steel of 19 ppm/°C, this would give up to ∼ 0.6 mm of slack between the center and the edge. In the worst case this would result in a vertical deviation of 2.4 mm in cross section, giving a potential angle of up to 13.5° relative to a flat grid. This was modeled with the 0.4 mm resolution of our SIMION 8.0 model as six concentric sections for the acceleration grid, which has by far the strongest effect on the ion trajectories. The instrumental fractionation pattern, determined using heavy ion differential streaming, is shown in Fig. 11 to be almost identical to the other cases, this time with a slightly decreased up-turn at the outer edge of the target.

Fig. 12 Helium isotopic
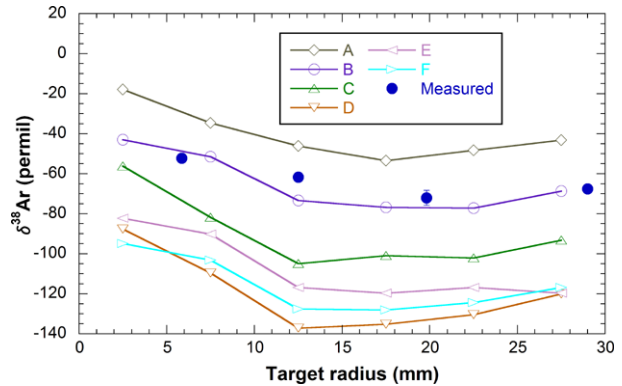fractionation measured (Heber
et al. 2011) and simulated
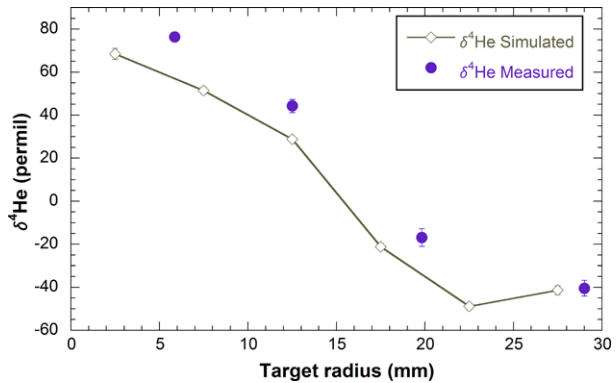
Concentration factors are given in Table 3 for all of the species discussed here. The averaged ^{16}O concentration factor predicted by Wiens et al. (2003) was 20.9x for SiC target material. Table 3 shows average concentration factors between 19.6 and 19.9 for nitrogen through neon. Lower concentration factors are shown for the heavier elements, S and Ar, to be discussed later. The overall concentration factor did not change by more than one percent with any of the different features tested for oxygen (Fig. 11), nor was the overall enhancement pattern changed as a function of radius. The comparison with measured concentrations is discussed below.

6.3 Measured Versus Simulated He and Ar

In addition to neon, the Concentrator simulations can be compared with measured isotopic patterns for two special cases: helium and argon (Heber et al. 2011). These two are special because of their low and high masses, which are respectively below and above the masses for which the Concentrator was planned. These elements were easily measured in the Concentrator targets because, being noble gases, they could be extracted, purified, and analyzed without contamination. The m/q ratio for ^{3}He is only 1.5, well below the minimum of 2.0 for which the instrument was designed. At this ratio, the light He isotope reflects too far above the solid mirror surface and is strongly influenced by the waffle pattern of the domed grid, resulting in angular scattering. The result is shown in Fig. 12, where the relative ^{3}He deficiency near the center of the target results in strong fractionation there. The figure shows that the modeled and measured fractionation patterns match each other relatively well, though the measured result is isotopically heavier than the model, similar to the neon result in Fig. 10. In spite of the strong fractionation gradient, the model predicts that, averaged over the entire target, the model-predicted overall instrumental fractionation for $^{4}He/^{3}He$ is not very high, at 2.9 ± 0.6 ‰ relative to unconcentrated solar wind (Table 4). This is in relative agreement with measurements, which found the integrated $^{4}He/^{3}He$ of the Concentrator target to be within 7 ‰ of the unconcentrated solar wind $^{4}He/^{3}He$ (Heber et al. 2011).

For argon, the mean m/q for mass 38 is in the range of 4.2–4.6 (Table 3), above the m/q range for which the instrument was designed. As m/q increases in going to successively heavier elements, the first effect is a loss of high-speed heavy-isotope ions due to impacts with the mirror over the velocity range where the mirror no longer tracks with the solar wind speed (>666 km/s). At sufficiently high m/q, e.g., greater than ~ 4.3, ions will also impact the mirror at lower solar-wind speeds. Figure 13 shows the measured results in comparison

Fig. 13 Measured δ^{38}Ar compared with simulations with various parameter values: A = 1.5 MK freezing in temperature, Gaussian, no heavy ion differential streaming; B = same with 1.2 MK; C = 1.5 MK, heavy ion differential streaming, no Gaussian; D = same with 1.2 MK; E = 1.5 MK Gaussian, heavy ion differential streaming; F = same with 1.2 MK


with several different simulations (discussed later). The mean fractionation for the simulation that agrees best with the measured data (Heber et al. 2011) is δ^{38}Ar $= -67$ ‰, obtained using a Gaussian distribution without heavy ion differential streaming and with a charge state distribution obtained from a 1.2 MK freeze-in temperature.

7 Discussion

7.1 Differences Between Modeled and Measured Results

The main difference between measured and modeled fractionation curves is that the modeled ones do not display as large overall ranges as the measurements. The models show slightly lower fractionation in the inner 10 mm, though the trend towards decreasing fractionation seen in the measurements is imitated there. All of the models show a leveling off or slight increases in the heavy isotopes beyond a radius of 20 mm on the target, which is not observed in the measurements of neon (Fig. 10) and helium (Fig. 12; Heber et al. 2011). The stronger fractionation near the target's center could likely be imitated in the model by adjusting slightly, within uncertainties, towards a tighter solar-wind angular distribution (Fig. 8). The ions implanted in the outer 10 mm of the target have a relatively low concentration (Table 3) and so they are not as important for solar-wind measurements as the ions implanted in the inner two centimeters (see McKeegan et al. 2011). However, we still wish to know the reason for the discrepancy. Each simulation presented in Tables 3 and 4 consists of five different runs per isotope at different velocities and corresponding instrument potentials. To obtain the results in these tables the velocity bins are each weighted by the proportion of solar wind in each velocity bin determined for oxygen by ACE over the time period the Concentrator was operating. The individual velocity runs are shown for Ne in Fig. 14. One can see that they all follow a similar downward trend with increasing radius, but that the lowest velocity bin (350 km/s) shows a very strong positive fractionation towards the outer edge of the target, while the other bins generally level off in the last 10 mm in radius. It is likely that the 350 km/s fractionation is over-emphasized in the overall fractionation pattern because of the way the velocity bins were defined. Each run was centered over the 100 km/s region it was to represent. However, this region of velocity space represents the rising edge of the distribution curve, as most of the ions (70 %) in the 300–400 km/s velocity bin have $v > 350$ km/s and will in reality behave somewhat more like the 450 km/s curve, which is flat in the outer 10 mm of the target.

Fig. 14 Simulated neon fractionation factors for each velocity bin as a function of target radius
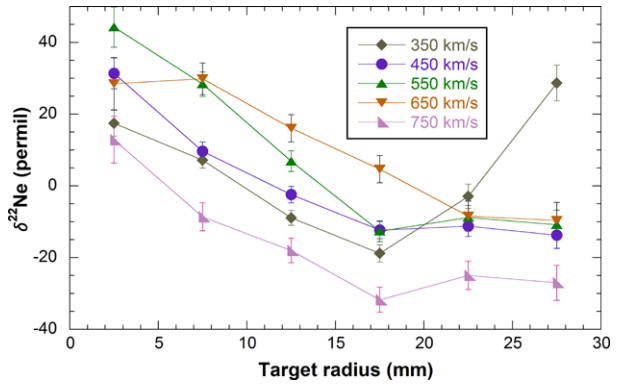
Fig. 15 Ion angular distribution near the outer edge of the target for 350 km/s oxygen normally incident on the Concentrator
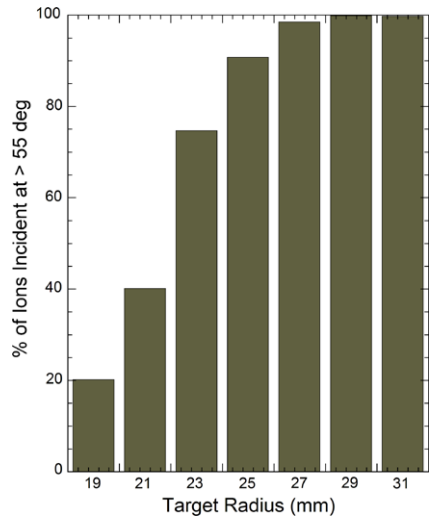
A second potential reason for differences between the model and measured observations involves electrostatic effects at the edge of the Concentrator. As might be expected from the high incidence angles, tracing the ions back to the mirror shows that a large fraction of the ions incident on the outer centimeter of the target come from the outer edges of the Concentrator. Electrostatic instruments like the Concentrator often have boundary-condition effects in which the structure outside of the ion flight region affects electric fields in this region in ways that are either not well known or are not well modeled. Lower-speed ions are more susceptible to edge effects, consistent with Fig. 14. We therefore consider it likely that the difference between predicted and measured fractionation near the edge of the target is due to edge effects in the instrument itself, magnified by the high angle of incidence of these ions on the target (Fig. 15). The discrepancy is not due to the angular distribution of ions as they approach the Concentrator, as a simulation using normally incident ions shows the same effect in the outer 10 mm of the target.

Finally, we note that the oxygen isotopes (McKeegan et al. 2011, supporting online material), in contrast to Ne, showed evidence for a leveling off of the isotopic trend for measurements made in the outer centimeter of the target, which is consistent with the model results for speeds of 450 km/s and above. However, the relatively large uncertainties render the

data also consistent with a slight continued downward trend. Further, there is no compelling reason that the different elements in the same mass range should behave differently.

One additional factor must be considered in comparing simulated and measured fractionation patterns. The simulations assume that there is no isotope fractionation between slow and fast solar wind when in fact, a fractionation has been clearly measured for the noble gases from Genesis, at ∼ 63 ‰ for He and ∼ 4.2 ‰/amu for Ne (Heber et al. 2012). Wiens et al. (2003) presented data on the relative contribution of different solar wind velocities to different regions of the target. An updated table of these values is given in Table S5 in the supporting online material. In general the slower speeds are more sharply peaked towards the center of the target and contribute by far the most there. When this distribution is convolved with the observed fractionations mentioned above, they result in ∼ 10 ‰ difference for δ^4He between inner and outer portions of the target, somewhat consistent with the difference at small radial distances in Fig. 12. However, when the observed fast-slow fractionation is applied to other elements the difference is far more subtle, resulting in ∼ 0.5 ‰/amu difference between the inner and outer portions of the target for Ne, for example.

Concentration factors were reported for He, Ne, and Ar as a function of target radius by Heber et al. (2011). In each case the enhancements 3–6 mm from the center were ∼ 20 % lower than predicted, i.e., with a maximum of 43x compared with predicted concentrations of 58x and 52x for Ne in the 0–5 and 6–10 mm radial bins (Table 3). The difference between measured and predicted concentration decreases with increasing target radius, such that the observed enhancements at $r > 20$ mm meet the predictions. The reason for the difference is not clear. During development of the Concentrator significant attention was paid to grid scattering, in which the trajectory of an ion passing very close to a grid wire is bent significantly. However, narrow-beam tests with the instrument yielded sharp beam images on a detector located at the target position, largely ruling out significant grid scattering (Nordholt et al. 2003). At the same time, these tests also yielded beam positions farther from center than expected on average, potentially consistent with the current results, but for reasons that are not clear.

7.2 Fractionation Patterns for Elements Li-Mg in SiC

One question addressed in Heber et al. (2011) was whether the instrumental fractionation of oxygen and nitrogen is identical to that measured for neon. That question is revisited here in light of the simulations and is extended to other elements including Li and the heavier elements, Mg, Si, and S. For this discussion we ignore the discrepancy in the outer 10 mm of target radius while we investigate predicted fractionation differences between the elements. The fact that helium and to some extent argon are relatively well predicted by simulations gives reasonable confidence for predicting the relative instrumental fractionation of elements in between these mass ranges. Elements Li through Mg will be discussed first, and then the heavier elements, Si and S will be considered, returning to carbon implanted into silicon at the end.

Looking at Table 4 and Figs. 10, 12, and 13, it is clear that the lighter elements have steeper fractionation patterns than heavier elements. However, this difference is due to the larger relative mass separation for the lighter elements. Figure 16 shows the isotopic fractionation patterns in terms of permil/amu (top) and additionally, normalized to the mass difference of the element relative to oxygen (bottom). For example, the ^{7}Li/^{6}Li fractionations in Table 4 are scaled by a factor of 6.5/16.5 and ^{4}He/^{3}He by 3.5/16.5. To first order all of the elements He through Mg now have the same fractionation pattern. In finer detail there is a minor difference between He and Li on the one hand and the remaining elements. The

Fig. 16 Predicted instrumental fractionations as a function of Concentrator target radius for 5 mm radial bins. The fractionations are given in permil/amu (*top*) and also normalized for relative isotopic mass difference to oxygen (*bottom*, see text). *Error bars* provide statistical uncertainties
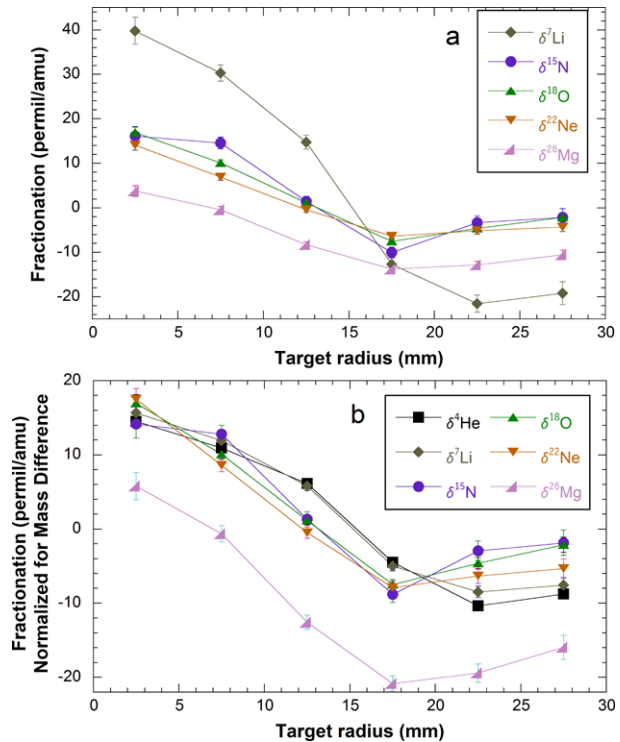
similarity between He and Li is a little surprising because their absolute m/q ranges differ significantly, at 1.5–2.0 for ^{3}He-^{4}He and 2.0–2.3 for Li. However, these two elements have in common a large difference in m/q between their two respective isotopes, which probably causes the slight difference relative to the heavier elements. One other second-order difference in Fig. 16 is a slightly lower overall trend for Mg. This will be discussed along with Si and S in a later section. Note that the curves in Fig. 16 include corrections due to backscattering losses at the target, which is a separate physical phenomenon from the Concentrator's ion optics.

7.3 Prognosis for Deuterium and Lithium

Deuterium was completely destroyed in the early Sun. However, measurements have been attempted from time to time in order to determine limits on D which may have been contributed to the photosphere and solar wind either by late infall of cometary material or by spallation reactions in the corona. Extrapolations of lunar soil measurements placed an upper limit on solar-wind D/H of $< 3 \times 10^{-6}$ (Epstein and Taylor 1972, 1973). A recent analysis of unconcentrated Genesis samples found a better upper limit, on the order of $< 2 \times 10^{-7}$ (Huss et al. 2012). The Concentrator enhances the fluence of D by up to 40x, as its m/q ratio is 2.0, the same as ^{16}O^{+8}, and at the same time the instrument removed about 85 % of the H ($m/q = 1.0$) with the positive-potential grid. The remaining H has a different abundance pattern on the target, as the low m/q causes the protons to reflect relatively far above the mirror electrode where the influence of the waffle pattern of the domed grid tends to scatter the ions across the target instead of focusing them toward the center. Using a Concentrator target for a D/H analysis should result in at least a 40x improvement in the D/H upper limit

based on the enhancement of D. If the relative reduction of H in the target, particularly near the center, also aids in detection of D, the upper limit might be further improved. One would need to correct any result obtained on the target by both the instrumental enhancement of D and the reduction of H, as well as losses or fractionation due to backscatter at the target, which could be significant.

Lithium represents a very interesting potential observation for solar physics because at sufficient temperatures in the Sun it is depleted, but likely not completely destroyed, by reactions with protons. The minimum temperature for this reaction differs for the two stable isotopes from $\sim 2 \times 10^6$ K for ^{6}Li to $\sim 20\%$ higher for ^{7}Li (e.g., Stix 2004). The standard solar model may be consistent with complete destruction of solar Li during the pre-main-sequence time when the solar convection zone extended deeper. Photospheric absorption line observations provide Li abundance estimates of 1.02 ± 0.12 DEX (Ritzenhoff et al. 1997) and 1.05 ± 0.2 (Baranovsky and Tarashchuk 2008) which are approximately factors of 200 below that estimated from meteoritic abundances (e.g., Asplund et al. 2009), consistent with significant destruction of Li in the Sun. Using the measured H fluence integrated over the exposure duration of the Concentrator (1.9×10^{16} cm^{-2}), and converting the 1.05 DEX to a Li/H ratio of 1.1×10^{-11}, the expected unconcentrated Li abundance is 2.1×10^5 cm^{-2} or a maximum of 6.3×10^5 atoms/cm^2 if the solar wind Li/H is enriched by a factor three relative to photosphere due to the first ionization potential (FIP) effect. The Concentrator target enriched elements from He to Ne by a factor of 40 in the inner 6 mm radial area (Heber et al. 2011). The current best estimate of the photospheric ^{6}Li/^{7}Li ratio is ≤ 0.03 (Ritzenhoff et al. 1997). Thus expected abundances to be measured in the inner 6 mm of the concentrator target are up to 2.5×10^7 ^{7}Li/cm^2 and $\leq 7.6 \times 10^5$ ^{6}Li/cm^2, which translates into total amounts of atoms of 2500 (^{7}Li) and ≤ 76 (^{6}Li) in a 100×100 μm^2 raster, a general raster size used for SIMS analysis. The relative sensitivity of Li in Si sputtered by an O beam is high, the useful yield (number of ions detected/number of atoms sputtered) is between 10 and 50 % (e.g. Wilson 1995). Thus, in principle, using the combined data from numerous rasters, as was done for the much more precise O and N measurements (McKeegan et al. 2011; Marty et al. 2011), a low-precision Li isotopic measurement of Genesis-collected solar wind could be feasible in the innermost area of the concentrator target in absence of Li surface contamination, however, it yet has to be tested.

7.4 Heavy Element Analyses

While the Concentrator was originally conceived, designed, and operated for elements lighter than or equal to neon, there is a strong desire to utilize the Concentrator for analyses of heavier elements if possible. Magnesium is a non-volatile, low first-ionization-potential element, the isotopic ratios of which are constant to within ± 0.04 ‰ for ^{26}Mg/^{24}Mg for igneous samples and meteorites within the inner solar system (Chakrabarti and Jacobsen 2010). It is expected to be incorporated into the Sun without any of the isotopic fractionations seen in volatile elements O (McKeegan et al. 2011) and N (Marty et al. 2011). As such, Mg may be the best element to precisely determine solar wind isotopic fractionation (e.g., Kucharek et al. 1997; Kallenbach et al. 1998). Another element of particular isotopic interest is sulfur. Given the large scale isotopic differences between the Sun and Earth for volatile elements oxygen and nitrogen (McKeegan et al. 2011; Marty et al. 2011), sulfur, as another volatile element, may also display unexpected isotopic fractionation. In contrast to N and O, the sulfur isotopic variations in meteorites are more subtle, in the range of -7.3 ‰ $\leq \delta^{34}$S ≤ 6.1 ‰ for carbonaceous chondrites, but with a total range of less than one permil for ordinary chondrites and just over two permil for achondrites, as summarized in Rai and Thiemens (2007).

Fig. 17 Predicted sulfur isotopic fractionation as a function of target radius for each of the velocity bins used in the simulations
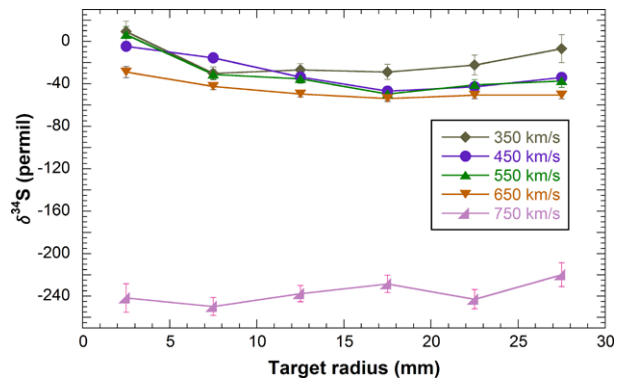
It is already clear from an earlier discussion that argon is severely fractionated because its mass-to-charge ratio is too high to achieve one hundred percent reflection by the electrostatic mirror. The question we address here is whether the Concentrator targets can provide accurate isotopic results for these elements of intermediate mass between Ne and Ar. As provided in Table 2, the mean mass per charge ratio rises quite steeply from Mg (2.8) to Si (3.6) and S (4.1), which is almost as high as that of Ar (4.4).

As mentioned earlier, the mirror's voltage tracks the kinetic energy of the incoming protons to a speed of 667 km/s, at which point the maximum potential of 10 kV is reached. As the solar wind velocity increases above this point, ions reflect closer and closer to the mirror until at some point high m/q ions begin to be lost due to collisions with the mirror. This results in particularly strong isotopic fractionation, as the heavier isotope always has a slightly higher m/q than the lighter isotope. For most of the mission a cut-off proton speed of 800 km/s was used. The highest velocity bin of the simulations (700–800 km/s) is the most susceptible to fractionation for heavy ions, and non-mass-dependent fractionation can result.

Because of this operational limitation of the Concentrator, the issue of differential streaming is important for the heavy ions. However, there appears to be a disagreement within the literature and current observations regarding differential streaming of ions heavier than neon. On the one hand, some observations (e.g., Schmid et al. 1987; Bochsler 1989; Wurz 2001) clearly indicate that these heavy ions travel more slowly than He, consistent with no differential streaming relative to protons for the heaviest species, e.g., Si through Fe, at relatively high speeds. On the other hand, data from ACE SWICS over the Concentrator collection time period, and in general (Berger et al. 2011), do not indicate any differences between these elements and helium, i.e., with a differential streaming relative to protons. Because it gave the best match for argon (Fig. 13), we modeled Si and S with no differential streaming relative to protons.

Figures 17 and 18 show the results for Si and S, respectively, for each velocity bin. It is clear that a significant fraction of the ions are lost from the highest-velocity bin, resulting in increasingly strong fractionation, into the hundreds of permil. For sulfur enough low-charge-state ions are lost from the other velocity bins to pull their mean contributions below zero permil as well. The resulting mean fractionation given in Table 4 drops to -18.3 ± 1.1 ‰ for δ^{30}Si and to -44.6 ± 1.2 ‰ for δ^{34}S, where the quoted uncertainty is merely the statistical accuracy and does not reflect other potential issues with the model. The overall uncertainty is likely to be on the order of five or up to ten times the statistical uncertainty, based on comparison with the neon and argon measurements. Table 3 shows that, in spite

Fig. 18 Predicted silicon isotopic fractionation as a function of target radius for each of the velocity bins used in the simulations
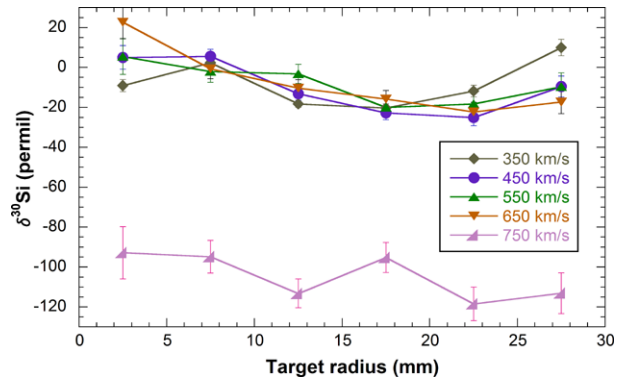
of the isotopic fractionation, the overall concentration factor is reduced by only about 5 %. Thus, it appears possible to use the Concentrator targets to obtain a measurement of the S isotopic composition in the Sun by correcting the data using the model results reported here. Although the accuracy will not be as good as that of the elements for which the Concentrator was intended (e.g., O, N, Ne), such a measurement may still be quite useful, as it would clearly distinguish solar-terrestrial isotopic differences of the order observed for oxygen (McKeegan et al. 2011) and nitrogen (Marty et al. 2011) with an accuracy better than ±1 %.

Magnesium is an intermediate case between the mass range intended for use and the heavy elements which are clearly fractionated, and here the heavy ion differential streaming is critical. Wurz (2001), noting that in his data set the differential streaming drops off significantly between oxygen and silicon, interpolated between these elements to predict differential streaming values of −6, +1, +8, +15, and +22 km/s for Mg at the 350–750 km/s increments used in the model. These inputs result in relatively minor overall fractionation on the Concentrator target. The 750 km/s run yielded a mean fractionation of δ^{26}Mg = −38 ‰, which is considerable, but far less than those of Si, S, and Ar at this speed. A velocity-averaged mean δ^{26}Mg of −3.7 ‰ is obtained, which is only a −1.6 ‰/amu correction relative to the prediction for the carefully-measured neon fractionation (Heber et al. 2011). However, it seems more prudent to use the differential streaming obtained by ACE for the time period over which the Concentrator was operating, in which Mg appears to stream with He. Using these velocities, the highest velocity bin is fractionated by −57 ‰, averaged across the target. The velocity-averaged results are given in Table 4 for each radial bin, and results in a spatially averaged value of δ^{26}Mg = −15.7 ‰. Given the uncertainty in differential streaming discussed above, the Concentrator targets may not be highly useful for determining the precise isotopic composition of solar-wind Mg. Note that the instrumental fractionation of Mg and the heavier elements including Si and S are likely to be slightly non-mass-dependent due to the preferential loss of the heaviest ion at the mirror electrode in the high speed wind. Backscatter losses have a negligible effect on the ratios of these isotopes.

7.5 Carbon Analyses

Carbon analysis in the Concentrator was thought to be impossible due to its presence as a major constituent in all of the target materials. However, the diamond-on-silicon target (Jurewicz et al. 2003) has several small areas in which the diamond-like carbon coating appears absent. One such region is seen as a narrow rectangle at the eleven o-clock position in Fig. 3.

Comparison with pre-flight images of the target assembly appears to confirm that this area was uncoated before the flight, likely due to the position of a clip holding the sample during carbon coating. Careful inspection of this quadrant indicates surface features consistent with radiation damage not seen on the SiC quadrants (J. Allton, personal communication). These surface features are strong in the largest bare Si region at 0–10 mm radius (Fig. 3) but do not appear to be present in another bare region near the outer radial edge of the target. The presence of bare silicon allows the possibility that the Concentrator could be used to analyze carbon isotopes, likely in the bare region near the perimeter. For this reason, carbon ions were modeled as well and the results are given in Tables 3 and 4. The carbon results were not included in any of the figures comparing the various fractionation curves due to the fact that this element is modeled in a different substrate, that is, in pure Si.

The carbon results in Table 4 are somewhat surprising in that the fractionation pattern, as well as the target-wide average, is isotopically light compared to what might be expected from interpolation between the lighter and heavier elements, Li, N, and O. All of the difference can be accounted for in the 700–800 km/s velocity bin, the curve for which drops as low as -37 ‰ for some radial bins. While a relatively small fraction of ions are in this velocity bin, it is enough to pull the velocity-averaged fractionation down approximately 3 ‰ for each of the radial bins in Table 4, and resulting in a target-averaged fractionation of -1.0 ‰. The reason is the relatively high fraction of carbon in the +4 charge state for this velocity range (24 %; Table 1). The ^{13}C kinetic energy at an incoming velocity of 790 km/s (used to represent the 700–800 km/s velocity bin with differential heavy ion streaming) is 42 keV, which at +4 charge is slightly incompatible with the maximum 10 kV potential of the mirror. Note that N, O, and Ne all have charge states yielding higher m/q values (Table 1), but the fraction of ions at these charge states is very minor, much less than for carbon. If the carbon is modeled without differential streaming (i.e., using a velocity of 750 km/s to represent the 700–800 km/s proton velocity bin), the fractionation curve is more as expected relative to Li, N, and O, with a target-averaged fractionation of $+2.2 \pm 0.6$ ‰. The actual value expected for carbon is most likely between these two values, as the larger fraction of ions in the 700–800 km/s velocity bin is weighted towards the lower energy side in the absence of differential streaming. Comparison of the mean fractionation value with these other elements should provide insight into the expected fractionation relative to He and Ne in the bare silicon region, as these elements were measured in equivalent radial positions on another quadrant (Heber et al. 2011).

8 Summary

Already we can conclude that the Genesis Solar Wind Concentrator has performed well beyond expectations, particularly in light of the hard landing of the capsule, which prevented a post-flight re-calibration of the instrument or even visual analysis of the grids in the state they had been during operation in flight. This work explained in detail the features observed in the elements analyzed from its targets to date, and defines the limitations and opportunities that lie ahead for future analyses. In particular, thanks to noble gas measurements (Heber et al. 2011), instrumental fractionation is known with high confidence for all isotopes between ^3He and ^{22}Ne and may facilitate future analyses of Li and C in the Concentrator targets. Isotopes of S, Si, and to some extent, Mg, are more significantly fractionated by losses due to impact with the mirror electrode, as corroborated by Ar analyses (Heber et al. 2011), but could still be analyzed. Surprisingly, very slight losses appear to affect C in a minor way as well, due to the abundance of its +4 charge state in high-speed wind. The

issue of differential fractionation between fast and slow solar wind affects the distribution of helium isotopes on the target, but should have a negligible effect on heavier elements.

References

J.H. Allton, M.J. Calaway, M.C. Rodriguez, Preliminary quantification of image color gradient on Genesis concentrator silicon carbide target 60001. Lunar Planet. Sci. **XXXIX**, 1440 (2008)

M. Asplund, N. Grevesse, A.J. Sauval, P. Scott, The chemical composition of the Sun. Annu. Rev. Astron. Astrophys. **47**, 481–522 (2009)

S.K. Atreya, P.R. Mahaffy, H.B. Niemann, M.H. Wong, T.C. Owen, Composition and origin of the atmosphere of Jupiter—an update, and implications for the extrasolar giant planets. Planet. Space Sci. **51**, 105–112 (2003)

E.A. Baranovsky, V.P. Tarashchuk, Lithium abundances in sunspots. Bull. Crimean Astrophys. Obs. **104**, 19–25 (2008). Translated from original Russian text in Izv. Krymskoi Astrofiz. Obs. **104**, 31–40

B.L. Barraclough, E.E. Dors, R.A. Abeyta, J.F. Alexander, F.P. Ameduri, J.R. Baldonado, S.J. Bame, P.J. Casey, G. Dirks, D.T. Everett, J.T. Gosling, K.M. Grace, D.R. Guerrero, J.D. Kolar, J.L. Kroesche Jr., W.L. Lockhart, D.J. McComas, D.E. Mietz, J. Roese, J. Sanders, J. Steinberg, R.L. Tokar, C. Urdiales, R.C. Wiens, Genesis electron and ion spectrometers. Space Sci. Rev. **105**, 627–660 (2003)

R.H. Becker, Solar wind ^{15}N/^{14}N from Genesis—a tale of two values. Lunar Planet. Sci. **XLI**, 2469 (2010)

L. Berger, R.F. Wimmer-Schweingruber, G. Gloeckler, Systematic measurements of ion-proton differential streaming in the solar wind. Phys. Rev. Lett. **106**, 151103 (2011)

P. Bochsler, Velocity and abundance of silicon ions in the solar wind. J. Geophys. Res. **94**, 2365–2373 (1989)

P. Bochsler, Minor ions in the solar wind. Astron. Astrophys. Rev. **14**, 1–40 (2007)

P. Bryans, N.R. Badnell, T.W. Gorczyca, J.M. Laming, W. Mitthumsiri, D.W. Savin, Collisional ionization equilibrium for optically thin plasmas. I. Updated recombination rate coefficients for bare through sodium-like ions. Astrophys. J. Suppl. Ser. **167**, 343–356 (2006)

D.S. Burnett, B.L. Barraclough, R. Bennett, M. Neugebauer, L.P. Oldham, C.N. Sasaki, D. Sevilla, N. Smith, E. Stansbery, D. Sweetnam, R.C. Wiens, The Genesis Discovery mission: return of solar matter to Earth. Space Sci. Rev. **105**, 509–534 (2003)

D.S. Burnett, K.M. McNamara, A. Jurewicz, D. Woolum, Molecular contamination on anodized aluminum components of the Genesis science canister. Lunar Planet. Sci. **XXXVI**, 2405 (2005)

M.J. Calaway, E.K. Stansbery, K.M. McNamara, Modeling ellipsometry measurements of molecular thin-film contamination on Genesis flown array samples. Lunar Planet. Sci. **XXXVII**, 1420 (2006)

M.J. Calaway, M.C. Rodriguez, E.K. Stansbery, Genesis silicon carbide concentrator target 60003 preliminary ellipsometry mapping results. Lunar Planet. Sci. **XXXVIII**, 1632 (2007)

M.J. Calaway, M.C. Rodriguez, J.H. Allton, Genesis Concentrator target particle contamination mapping and material identification. Lunar Planet. Sci. **XXXIX**, 1423 (2008)

R. Chakrabarti, S.B. Jacobsen, The isotopic composition of magnesium in the inner solar system. Earth Planet. Sci. Lett. **293**, 349–358 (2010)

R.N. Clayton, Oxygen isotopes in meteorites. Annu. Rev. Earth Planet. Sci. **21**, 115–149 (1993)

R.N. Clayton, Self-shielding in the solar nebula. Nature **415**, 860–861 (2002)

R.N. Clayton, T.K. Mayeda, The oxygen isotope record in Murchison and other carbonaceous chondrites. Earth Planet. Sci. Lett. **67**, 151–161 (1984)

R.N. Clayton, N. Onuma, L. Grossman, T.K. Mayeda, Distribution of the pre-solar component in Allende and other carbonaceous chondrites. Earth Planet. Sci. Lett. **34**, 209–224 (1977)

D.A. Dahl, SIMION for the personal computer in reflection. Int. J. Mass Spectrom. **200**, 3–25 (2000)

S. Epstein, H.P. Taylor Jr., O^{18}/O^{16}, Si^{30}/Si^{28}, C^{13}/C^{12}, and D/H studies of Apollo 14 and 15 samples, in *Proc. 3rd Lun. Sci. Conf. (Supplement 3, Geochim. Cosmochim. Cosmochim. Acta)* (MIT Press, Cambridge, 1972), pp. 1429–1454

S. Epstein, H.P. Taylor Jr., The isotopic composition and concentration of water, hydrogen, and carbon in some Apollo 15 and 16 soils and in the Apollo 17 orange soil, in *Proc. 4th Lun. Sci. Conf. (Supplement 4, Geochim. Cosmochim. Acta)* (Pergamon, New York, 1973), pp. 1559–1575

T. Fouchet, E. Lellouch, B. Bezard, T. Encrenaz, P. Drossart, H. Feuchtgruber, T. de Graauw, ISO-SWS observations of Jupiter: measurement of the ammonia tropospheric profile and of the N-15/N-14 isotopic ratio. Icarus **143**, 223–243 (2000)

I.A. Franchi, I.P. Wright, C.T. Pillinger, Heavy nitrogen in Bencubbin—a light-element isotopic anomaly in a stony-iron meteorite. Nature **323**, 138–140 (1986). doi:10.1038/323138a0

J. Geiss, F. Bühler, H. Cerutti, P. Eberhardt, C. Filleux, J. Meister, P. Signer, The Apollo SWC experiment: results, conclusions, consequences. Space Sci. Rev. **110**, 307–335 (2004)

G. Gloeckler, J. Geiss, The composition of the solar wind in polar coronal holes. Space Sci. Rev. **130**, 139 (2007)

G. Gloeckler, J. Cain, F.M. Ipavich, E.O. Turns, P. Bedini, L.A. Fisk, T.H. Zurbuchen, P. Bochsler, J. Fischer, R.F. Wimmer-Schweingruber, J. Geiss, R. Kallenbach, Investigation of the composition of solar and interstellar matter using solar wind and pickup ion measurements with SWICS and SWIMS on the ACE spacecraft. Space Sci. Rev. **86**, 497–539 (1998)

V.S. Heber, R.C. Wiens, A.J.G. Jurewicz, H. Baur, N. Vogel, R. Wieler, D.S. Burnett, Isotope fractionation of solar wind implanted into the Genesis Concentrator target determined by neon in the gold cross and implantation experiments. Lunar Planet. Sci. **XL**, 1485 (2009)

V.S. Heber, R.C. Wiens, A.J.G. Jurewicz, N. Vogel, H. Baur, K. McKeegan, R. Wieler, D.S. Burnett, Genesis Concentrator target: isotopic and elemental fractionation of implanted solar wind characterized and quantified by noble gases. Meteorit. Planet. Sci. (2011). doi:10.1111/j.1945-5100.2011.01170.x

V.S. Heber, H. Baur, R. Wieler, P. Bochsler, D.S. Burnett, D.B. Reisenfeld, R.C. Wiens, Fractionation processes in the solar wind detected by Genesis: He, Ne, and Ar isotopic and elemental composition of different solar wind regimes. Astrophys. J. **759**, 121 (2012). doi:10.1088/0004-637X/759/2/121

S. Hefti, H. Grunwaldt, F.M. Ipavich, P. Bochsler, D. Hovestadt, M.R. Aellig, M. Hilchenbach, R. Kallenbach, A.B. Galvin, J. Geiss, F. Gliem, G. Gloeckler, B. Klecker, E. Marsch, E. Mobius, M. Neugebauer, P. Wurz, Kinetic properties of solar wind minor ions and protons measured with SOHO/CELIAS. J. Geophys. Res. **103**, 29,697–29,704 (1998)

G.R. Huss, K. Nagashima, D.S. Burnett, A.J.G. Jurewicz, C.T. Olinger, A new upper limit on the D/H ratio in the solar wind. Lunar Planet. Sci. **XLIII**, 1709 (2012)

A.J.G. Jurewicz, D.S. Burnett, R.C. Wiens, T.A. Friedmann, C.C. Hays, R.J. Hohlfelder, K. Nishiizumi, J.A. Stone, D.S. Woolum, R. Becker, A.L. Butterworth, A.J. Campbell, M. Ebihara, I.A. Franchi, V. Heber, C.M. Hohenberg, M. Humayun, K.D. McKeegan, K. McNamara, A. Meshik, R.O. Pepin, D. Schlutter, R. Wieler, The Genesis solar-wind collector materials. Space Sci. Rev. **105**, 535–560 (2003)

R. Kallenbach, F.M. Ipavich, H. Kucharek, P. Bochsler, A.B. Galvin, J. Geiss, F. Gliem, G. Gloeckler, H. Grünwaldt, S. Hefti, M. Hilchenbach, D. Hovestadt, Fractionation of Si, Ne, and Mg isotopes in the solar wind as measured by SOHO/CELIAS/MTOF. Space Sci. Rev. **85**, 357–370 (1998)

R. Kallenbach, K. Bamert, M. Hilchenbach, Isotopic composition of the solar wind inferred from in-situ spacecraft measurements. Space Sci. Rev. (2007). doi:10.1007/s11214-007-9216-0

A.P.A. Kallio, K.D. McKeegan, G. Jarzebinski, P.H. Mao, T. Kunihiro, C.D. Coath, V.S. Heber, D.S. Burnett, R.C. Wiens, Nitrogen isotopic composition of solar wind returned by the GENESIS mission. Lunar Planet. Sci. **XLI**, 2481 (2010)

J.F. Kerridge, Long-term compositional variation in solar corpuscular radiation: evidence from nitrogen isotopes in the lunar regolith. Rev. Geophys. **31**, 423–437 (1993)

J.H. King, N.E. Papitashvili, Solar wind spatial scales in and comparisons of hourly wind and ACE plasma and magnetic field data. J. Geophys. Res. **110**, A02104 (2005). doi:10.1029/2004JA010649

H. Kucharek, F.M. Ipavich, R. Kallenbach, P. Bochsler, D. Hovestadt, H. Grünwaldt, M. Hilchenbach, W.I. Axford, H. Balsiger, A. Bürgi, M.A. Coplan, A.B. Galvin, J. Geiss, G. Gloeckler, K.C. Hsieh, B. Klecker, M.A. Lee, S. Livi, G.G. Managadze, E. Marsch, E. Möbius, M. Neugebauer, K.U. Reiche, M. Scholer, M.I. Verigin, B. Wilken, P. Wurz, Magnesium isotope composition in the solar wind as observed with the MTOF sensor on the CELIAS experiment on board the SOHO spacecraft. ESA SP **404**, 473–476 (1997)

E. Marsch, K.H. Muhlhauser, H. Rosenbauer, R. Schwenn, F.M. Neubauer, Solar wind helium ions: observations of the Helios solar probes between 0.3 and 1 AU. J. Geophys. Res. **87**, 35–51 (1982)

B. Marty, L. Zimmermann, P.G. Burnard, D.S. Burnett, R.C. Wiens, V.S. Heber, R. Wieler, P. Bochsler, Nitrogen isotopes in the recent solar wind from the analysis of Genesis targets: evidence for large-scale isotope heterogeneity in the nascent solar system. Geochim. Cosmochim. Acta **74**, 340–355 (2010)

B. Marty, M. Chaussidon, R.C. Wiens, A.J.G. Jurewicz, D.S. Burnett, A ^{15}N-poor isotopic composition for the solar system as shown by Genesis solar wind samples. Science **332**, 1533–1536 (2011)

D.J. McComas, B.L. Barraclough, R.W. Moses, D.S. Burnett, R.C. Wiens, M. Neugebauer, Solar wind concentrator, in *Measurement Techniques for Space Plasmas*, ed. by R.F. Pfaff, J.E. Borovsky, D.T. Young. AGU Monograph, vol. 102 (1997), pp. 195–200

K.D. McKeegan, A.P.A. Kallio, V.S. Heber, G. Jarzebinski, P.H. Mao, C.D. Coath, T. Kunihiro, R.C. Wiens, J.E. Nordholt, R.W. Moses Jr., D.B. Reisenfeld, A.J.G. Jurewicz, D.S. Burnett, The oxygen isotopic composition of the Sun inferred from captured solar wind. Science **332**, 1528–1532 (2011)

J.E. Nordholt, R.C. Wiens, R.A. Abeyta, J.R. Baldonado, D.S. Burnett, P. Casey, D.T. Everett, W. Lockhart, D.J. McComas, D.E. Mietz, P. MacNeal, V. Mireles, R.W. Moses Jr., M. Neugebauer, J. Poths, D.B. Reisenfeld, S.A. Storms, C. Urdiales, The Genesis solar wind concentrator. Space Sci. Rev. **105**, 561–599 (2003)

T. Owen, P.R. Mahaffy, H.B. Niemann, S. Atreya, M. Wong, Protosolar nitrogen. Astrophys. J. **553**, L77–L79 (2001)

V.K. Rai, M.H. Thiemens, Mass independently fractionated sulfur components in chondrites. Geochim. Cosmochim. Acta **71**, 1341–1354 (2007)

D.B. Reisenfeld, R.C. Wiens, J.T. Steinberg, J. Raines, T. Zurbuchen, B.L. Barraclough, Solar wind conditions and composition during the Genesis mission as measured by in situ spacecraft. Space Sci. Rev. (2012). doi:10.1007/s11214-013-9960-2

S. Ritzenhoff, E.H. Schröter, W. Schmidt, The lithium abundance in sunspots. Astron. Astrophys. **328**, 695–701 (1997)

M.C. Rodriguez, M.C. Calaway, J.H. Allton, K.M. McNamara, J.D. Hittle, Status of reconstruction of fragmented diamond-on-silicon collector from Genesis spacecraft solar wind concentrator. Lunar Planet. Sci. **XL**, 1337 (2009)

S. Schläppi, K. Altwegg, H. Balsiger, M. Hässig, A. Jäckel, P. Wurz, B. Fiethe, M. Rubin, S.A. Fuselier, J.J. Berthelier, J. De Keyser, H. Rème, U. Mall, Influence of spacecraft outgassing on the exploration of tenuous atmospheres with in situ mass spectrometry. J. Geophys. Res. **115**, A12313 (2010). doi:10.1029/2010JA015734

J. Schmid, P. Bochsler, J. Geiss, Velocity of iron ions in the solar wind. J. Geophys. Res. **92**, 9901–9906 (1987)

R.M. Skoug, J.T. Gosling, J.T. Steinberg, D.J. McComas, C.W. Smith, N.F. Ness, Q. Hu, L.F. Burlaga, Extremely high speed solar wind. J. Geophys. Res. **109**, A09102 (2004). doi:10.1029/2004JA010494

M. Stix, *The Sun*, 2nd edn. (Springer, Berlin, 2004)

M.H. Thiemens, J.E. Heidenreich III, The mass-independent fractionation of oxygen: a novel isotope effect and its possible cosmochemical implications. Science **219**, 1073–1075 (1983)

R. Wieler, F. Humbert, B. Marty, Evidence for a predominantly non-solar origin of nitrogen in the lunar regolith revealed by single grain analyses. Earth Planet. Sci. Lett. **167**, 47–60 (1999)

R.C. Wiens, G.R. Huss, D.S. Burnett, The solar oxygen isotopic composition: predictions and implications for solar nebula processes. Meteorit. Planet. Sci. **34**, 99–108 (1999)

R.C. Wiens, M. Neugebauer, D.B. Reisenfeld, R.W. Moses Jr., J.E. Nordholt, Genesis solar wind concentrator: computer simulations of performance under solar wind conditions. Space Sci. Rev. **105**, 601–626 (2003)

R.C. Wiens, P. Bochsler, D.S. Burnett, R.F. Wimmer-Schweingruber, Solar and solar-wind isotopic compositions. Earth Planet. Sci. Lett. **222**, 697–712 (2004)

R.G. Wilson, SIMS quantification in Si, GaAs, and diamond—an update. Int. J. Mass Spectrom. Ion Process. **143**, 43–49 (1995)

P. Wurz, Heavy ions in the solar wind: results from SOHO/CELIAS/MTOF. Habilitation thesis, University of Bern, Switzerland, 2001

E.D. Young, S.S. Russell, Oxygen reservoirs in the early solar nebula inferred from an Allende CAI. Science **282**, 452–455 (1998)

E.D. Young, A. Galy, H. Nagahara, Kinetic and equilibrium mass-dependent isotope fractionation laws in nature and their geochemical and cosmochemical significance. Geochim. Cosmochim. Acta **66**, 1095–1104 (2002)

J.F. Ziegler, M.D. Ziegler, J.P. Biersack, SRIM—the stopping and range of ions in matter. Nucl. Instrum. Methods Phys. Res. B **268**, 1818–1823 (2010)